Gravity Wave–Fine Structure Interactions. Part I: Influences of Fine Structure Form and Orientation on Flow Evolution and Instability

DAVID C. FRITTS AND LING WANG

GATS Inc., Boulder, Colorado

JOSEPH A. WERNE

NorthWest Research Associates, Boulder, Colorado

(Manuscript received 12 February 2013, in final form 30 July 2013)

ABSTRACT

Four idealized direct numerical simulations are performed to examine the dynamics arising from the superposition of a monochromatic gravity wave (GW) and sinusoidal linear and rotary fine structure in the velocity field. These simulations are motivated by the ubiquity of such multiscale superpositions throughout the atmosphere. Three simulations explore the effects of linear fine structure alignment along, orthogonal to, and at 45° to the plane of GW propagation. These reveal that fine structure alignment with the GW enables strong wave–wave interactions, strong deformations of the initial flow components, and rapid transitions to local instabilities and turbulence. Increasing departures of fine structure alignment from the GW yield increasingly less efficient wave–wave interactions and weaker or absent local instabilities. The simulation having rotary fine structure velocities yields wave–wave interactions that agree closely with the aligned linear fine structure case. Differences in the aligned GW fields are only seen following the onset of local instabilities, which are delayed by about 1–2 buoyancy periods for rotary fine structure compared to aligned, linear fine structure. In all cases, local instabilities and turbulence primarily accompany strong superposed shears or fluid ''intrusions'' within the rising, and least statically stable, phase of the GW. For rotary fine structure, local instabilities having preferred streamwise or spanwise orientations often arise independently, depending on the character of the larger-scale flow. Wave–wave interactions play the greatest role in reducing the initial GW amplitude whereas fine structure shears and intrusions are the major source of instability and turbulence energies.

1. Introduction

Internal gravity waves (GWs) account for much of the vertical energy and momentum transport throughout the atmosphere. They also are major contributors to instability and turbulence processes extending from the surface into the thermosphere that result in GW dissipation, spectral evolution, energy and momentum deposition, induced mean motions, and turbulence mixing and transport. These influences arise because of their rapid vertical propagation, their significant energy and momentum fluxes, their amplitude growth with decreasing density, and the increasing tendency for various instabilities as amplitudes increase [see Fritts and Alexander (2003) for a review of these dynamics]. While there are instances where local instability dynamics appear to be driven by a single GW of large amplitude (and large vertical scale) in the absence of smaller-scale mean or GW structures, the frequent occurrence of turbulence in relatively thin layers suggests that instabilities and turbulence often arise because of superpositions of variable mean and GW motions that may span a range of spatial and temporal scales. This is surely true at lower altitudes [e.g., from the stable boundary layer (SBL) into the lower stratosphere], where GW vertical scales and group velocities are often relatively small, causing individual GWs to be unable to grow rapidly and achieve instability except near strong local sources or in larger-scale wind shears. At higher altitudes [e.g., in the mesosphere and lower thermosphere (MLT)], however, superposed GWs arising from many sources, having disparate spatial scales and frequencies, and achieving larger vertical

Corresponding author address: D. C. Fritts, GATS Inc./Boulder, 3360 Mitchell Lane, Boulder, CO 80301.
E-mail: dave@gats-inc.com

DOI: 10.1175/JAS-D-13-055.1

group velocities and amplitudes are often observed. In such environments, ''multiscale'' interactions can drive very different dynamics than arise owing to instabilities of individual and superposed GWs. It is these multiscale dynamics accompanying GW instability arising as a result of GW–fine structure (GW–FS) interactions that are the subject of this paper.

To establish the context for our examination of multiscale instability dynamics in this paper, we first review the extensive studies of GW instabilities to date. Multiple studies have established that GWs having small (and large) amplitudes exhibit systematic energy exchanges via resonant interactions, primarily parametric subharmonic instabilities (PSI) (e.g., Thorpe 1968; McEwan 1971; Orlanski 1972; Mied 1976; Drazin 1977; McComas and Bretherton 1977; McEwan and Plumb 1977; Phillips 1977, 1981; LeBlond and Mysak 1978; Orlanski and Cerasoli 1981; Yeh and Liu 1981; Klostermeyer 1982, 1991; Craik 1985; Müller et al. 1986; Vanneste 1995; Lombard and Riley 1996; Sonmor and Klaassen 1997; Benielli and Sommeria 1998; Staquet and Sommeria 2002; Koudella and Staquet 2006). Larger GW amplitudes enable additional, local instabilities, spectral energy transfers, vigorous GW breaking, turbulence, and/or divergent energy and momentum fluxes that account for their prominent roles throughout the atmosphere. Initial 3D studies at low Reynolds number (Re) and low resolution defined the primary modes of instability and the dynamics of the transitions to turbulence (Andreassen et al. 1994, 1998; Fritts et al. 1994, 1998; Fritts and Alexander 2003; Sutherland 2006a).

Subsequent studies addressed GW instabilities at higher Re than the initial GW breaking studies cited above, influences of a transverse shear, instabilities of inertia–GWs, the roles of optimal perturbations in defining GW instability structures and influences on the GW amplitude, and the competition between, and interactions among, 2D wave–wave interactions and local 3D instabilities for smaller and larger GW amplitudes (Fritts et al. 2003, 2006, 2009a,b; Bouruet-Aubertot et al. 1995; Achatz 2005, 2007; Achatz and Schmitz 2006a,b; Lelong and Dunkerton 1998a,b; Thorpe 1999). More recent studies examined instabilities accompanying GW–mean flow interactions and GWs at very large scales at high altitudes (Sutherland 2001, 2006a,b; Dosser and Sutherland 2011; Fritts and Lund 2011; Lund and Fritts 2012). Key results of these studies include the following: 1) GW ''breaking'' (suggesting ''convective'' overturning) can occur for $a < 1$ [where $a = u_0'/|c - U|$ and a, u_0', c, and U are the nondimensional GW amplitude (with $a = 1$ corresponding to a convectively neutral GW), horizontal velocity amplitude, horizontal phase speed, and mean wind, respectively], 2) wave–wave interactions can lead to local instability and turbulence at smaller GW amplitudes, 3) wave–wave interactions and local instabilities compete directly at larger GW amplitudes, 4) both convective and Kelvin–Helmholtz (KH) instabilities (KHI) occur at smaller and larger inertia–GW amplitudes, 5) ''self-acceleration'' and modulational instabilities arise because of mean-flow interactions, 6) turbulence cascades involve apparently identical vorticity dynamics across a wide range of Re, and 7) instability and turbulence can extend to high altitudes at lower Re (by several or many decades) than occur at lower altitudes.

The various theoretical and modeling studies performed to date have shown that GW instability character and growth rates are strong functions of GW amplitudes, intrinsic frequencies, environmental influences, Re, and the Richardson number (Ri) that characterize these flows. Of these, Re varies most dramatically because of the increase of kinematic viscosity ν by about 10^7 from the SBL to about 110 km. Consequently, realistic values of Re for the lower atmosphere are impossible to achieve at present with direct numerical simulations (DNSs) that explicitly resolve GWs, instability, and turbulence scales, except at very small GW scales. From a stability perspective, an artificially low Re places strong constraints on instability scales and growth rates and prevents exploration of the dynamics that would arise at a real Re. A sufficiently high Re, while not realistic for the lower atmosphere, can nevertheless enable nearly the same initial instability dynamics as expected at higher Re (Lombard and Riley 1996; Fritts et al. 2006, 2009a). Because ν increases more rapidly than GW wavelengths as altitude increases, relevant $\mathrm{Re} = \lambda_z^2/(\nu T_b)$ (where λ_z and $T_b = 2\pi/N$ are the GW vertical wavelength and mean buoyancy period, respectively) describing GW instability dynamics decrease with altitude and are now attainable numerically in the middle MLT and above.

We now review the motivations for broadening our exploration of GW instability dynamics to encompass GW–FS interactions. Evidence for potential multiscale influences on GW instability dynamics has increased dramatically as high-resolution profiling capabilities for winds, temperatures, and other dynamical parameters have advanced. Importantly, however, a number of key insights into these dynamics accompanied earlier measurements of similar features in oceans and lakes. These include 1) identification of the frequent occurrence of ''sheet and layer'' structures in temperature and humidity (and salinity in the oceans) and corresponding current profiles; 2) recognition of their contributions to, and implications for, instability dynamics and turbulent mixing; 3) an initial appreciation of GW contributions to such dynamics; and 4) exploration of the relation between overturning fluid depths (e.g., the Thorpe scale L_T) and the Ozmidov scale L_O, which separates turbulence scales from GW scales (e.g., Woods 1968, 1969; Woods and Wiley 1972; Thorpe 1977, 1987; Gregg and Briscoe 1979; Dillon 1982; Gregg et al. 1986; Seim and Gregg 1994). In the above, "sheets" and "layers" refer to thin regions of high stratification and thicker regions having weaker stratification, respectively, $L_T = \langle d'^2 \rangle^{1/2}$, where d' is the Thorpe displacement, angle brackets denote a suitable average in depth, and $L_O = (\varepsilon/N^3)^{1/2}$, where ε is the mechanical energy dissipation rate.

As in oceans and lakes, high-resolution in situ probes in the SBL, troposphere, and lower stratosphere have revealed the presence of layered or oscillatory structures in temperatures and horizontal winds suggestive of high-vertical-wavenumber GWs or remnants of previous mixing events spanning many spatial scales (e.g., Barat 1982; Tsuda et al. 1989; Dalaudier et al. 1994; Coulman et al. 1995; Balsley et al. 1998, 2003, 2012; Muschinski and Wode 1998; Mahrt 1999; Luce et al. 2002; Gavrilov et al. 2005; Kelley et al. 2005; Sorbjan and Balsley 2008; Fukao et al. 2011). Additional evidence of highly structured profiles suggestive of current or previous layered turbulence and mixing events is provided by in situ measurements of the temperature structure parameter C_T^2 and ε (e.g., Barat et al. 1984; A. Muschinski et al. 1999, personal communication; Balsley et al. 2006, 2012) and by strong layering in radar reflectivity believed to accompany the temperature sheets having high C_T^2 (e.g., Gossard et al. 1971, 1984, 1985; VanZandt et al. 1978; Eaton et al. 1995; Luce et al. 1995, 2001, 2007, 2008; Muschinski et al. 1999; Chau et al. 2000; Nastrom and Eaton 2001; Fritts et al. 2003, 2011, 2012; Franke et al. 2011; Fukao et al. 2011). Fine structure scales at lower altitudes increase with altitude owing to the 20-times increase of ν over the lowest three scale heights and the more significant role of propagating GWs (favoring larger scales) at the higher altitudes.

Similar evidence of sheets, layers, and FSs in the MLT is available from a variety of in situ and remote sensing instruments. Here, however, the increase of ν by about 10^4–10^7 in the MLT (at about 60–110 km) relative to the SBL yields significant increases in the smallest GW and turbulence scales expected at these altitudes. This allows MLT instruments yielding coarser vertical resolution to nevertheless define MLT dynamics at the smaller scales that are dynamically relevant. Minimum scales are largely a function of Re, and local GW instabilities do not occur for $\mathrm{Re_{min}} \sim 1000$ or less (Fritts et al. 2006). This implies a minimum GW λ_z leading to instability of $\lambda_z \sim (\mathrm{Re_{min}}\nu T_b)^{1/2}$ (e.g., $\lambda_z \sim$ 1–2 km at about 80–90 km), and increases of about 10^2–10^3 in the MLT relative to the SBL. Vertical shears of horizontal winds (due largely to GWs) are constrained roughly by $u'_z = du'/dz \sim N$ owing to KHI or GW breaking (Fritts and Alexander 2003), such that GW horizontal velocities vary as $u' \sim N\lambda_z/2\pi = \lambda_z/T_b$ and the more energetic GW scales play the larger roles. Relevant measurements defining sheets, layers, and FSs in the MLT include radar, in situ rocket, and falling-sphere temperature and wind measurements (e.g., Tsuda et al. 1990; Lübken et al. 2002; Rapp et al. 2002, 2004; Fritts et al. 2004; Goldberg et al. 2006; Wang et al. 2006), lidar measurements of MLT winds and temperatures (e.g., Fritts et al. 2004), and airglow observations of small-scale KHI and GW breaking structures near 90 km implying relatively shallow shear layers enabling these dynamics (e.g., Hecht et al. 2005; Li et al. 2005).

From our perspective, the measurements reviewed above provide compelling evidence that instabilities and turbulence throughout the atmosphere often arise from multiscale (or GW–FS) interactions that may have very different implications for GW, mean-flow, and turbulence evolutions than implied by idealized GW instability studies. We expect, for example, that such interactions will include 1) enhancements of local shears (yielding local KHI) by larger-scale GW shears, 2) local GW breaking where superposed GWs yield enhanced local amplitudes, and 3) a potential for increased resonant and off-resonant wave–wave interactions. Specific examples of these dynamics include 1) localized and descending KHI seen by radars and lidars from the SBL into the MLT (e.g., Eaton et al. 1995; Lehmacher et al. 2007; Pfrommer et al. 2009) and 2) spatially localized (e.g., several wavelengths), rather than extensive, KHI and GW breaking seen in many airglow observations (e.g., Yamada et al. 2001; Hecht et al. 2005). Direct observational evidence of wave–wave interactions among GWs is more challenging, given current measurement capabilities, but there is ample evidence for such interactions from the various modeling and laboratory studies cited above.

An initial DNS of GW–FS dynamics by Fritts et al. (2009c, hereafter F09c) considered the superposition of a monochromatic GW having a frequency $\omega = N/10$ and an amplitude $a = u'_0/c = 0.5$ and an oscillatory mean-FS streamwise velocity having a zero mean, an approximately 10-times-smaller vertical wavelength than the GW, and a maximum shear $U_z = 2N$ (with minimum $\mathrm{Ri} = N^2/U_z^2 = 1/4$). The DNS was performed with Re = 50 000 so as to allow instability and turbulence extending to very small spatial scales. The GW and FS fields were thus both stable individually at the onset (apart from very slow potential PSI of the GW), but their superposition yielded a minimum Ri ~ 1/8 and their subsequent mutual advection and flow deformation resulted in significant instability and turbulence having a strongly layered structure thereafter. Despite its simplicity, the results of this DNS provide a number of interesting insights into GW–FS interactions that may be relevant to more general superpositions of larger- and smaller-scale, and higher- and lower-frequency, motions throughout the atmosphere. Subject to the initial conditions employed in this study, these insights include the following: 1) instabilities and turbulence occur at vertical scales defined more by the FSs than by the GWs, 2) the major source of turbulence energy is FSs rather than the larger scale GW, 3) the GW amplitude decreases only slightly while FS shears are largely eradicated throughout two GW periods, 4) turbulence generation is intermittent and spatially localized following instability onset, and 5) layered turbulence accompanying various turbulence events leads to sheet and layer structures that closely resemble observations in lakes, oceans, and the atmosphere.

To achieve these DNS capabilities, F09c employed a number of idealizations of the GW–FS flow to minimize the computational requirements. These include 1) simulating a monochromatic GW and mean FS in a compact domain that is periodic in each direction containing only a single vertical wavelength of the GW, 2) aligning the domain along the GW phase structure to reduce its horizontal extent, and 3) imposing the superposed GW and FS together at time $t = 0$ rather than ramping the GW from zero in the presence of the undisturbed initial FS. Such idealizations have implications for the generality of the results. The compact domain places strong constraints on other motions that can be excited via nonlinear interactions, as all possible modes must be periodic in the domain (integer wavenumbers in each direction). This causes the spectrum of possible GWs (potentially with wavelengths comparable to or larger than the computational domain) to be more discrete than would be the case in a much larger domain or in the atmosphere. However, it also allows generation of GWs having large horizontal or vertical scales, just as a tilted domain allows for mean horizontal motions (Fritts et al. 2006). The initial superposition of a monochromatic GW and unperturbed FS also clearly differs from that that would arise from a GW packet with the same characteristics propagating into such a FS environment. Such idealizations nevertheless allow insights into dynamics of superposed flows that would otherwise require much larger computational resources.

Our goals here are to explore more fully the influences of FS orientation and character on GWs, instability, and turbulence evolutions arising in these flows. Section 2 describes our formulation of the problem and the numerical methods employed. Section 3 examines the implications of differing FS orientation and character for the GW and turbulence fields, respectively. Section 4 discusses our results in the context of observations at various altitudes. Finally, section 5 provides a summary of our results and our conclusions. A companion paper by Fritts and Wang (2013, hereafter Part II) addresses the turbulence dissipation fields, evolutions, and statistics and their implications for the identification of these dynamics in observations.

2. Model formulation

a. Problem specification

As in our previous studies of high-resolution GW breaking and GW–FS interactions (i.e., Fritts et al. 2009a,b; F09c), we solve the 3D nonlinear Navier–Stokes equations subject to the Boussinesq approximation in a Cartesian domain that is aligned along the phase of the large-scale GW (see details below). Nondimensionalizing with respect to a velocity $V = \lambda_z/T_b$, the GW λ_z, and T_b, these equations may be written as

$$\partial \mathbf{u}/\partial t + \mathbf{u}\cdot\nabla\mathbf{u} = -\nabla p + \mathrm{Ri}\theta\mathbf{z} + \mathrm{Re}^{-1}\nabla^2\mathbf{u}, \qquad (1)$$

$$\partial\theta/\partial t + \mathbf{u}\cdot\nabla\theta = (\mathrm{Pr}\times\mathrm{Re})^{-1}\nabla^2\theta, \qquad (2)$$

$$\nabla\cdot\mathbf{u} = 0. \qquad (3)$$

Here, $\mathbf{u} = (u, v, w)$ is the total velocity vector; p is pressure; θ is total potential temperature; the buoyancy frequency N is defined as $N^2 = (g/\theta_0)d\theta_0/dz = g\beta/\theta_0$; g, θ_0, and β are gravity, mean potential temperature, and mean potential temperature gradient, respectively; and $\mathbf{z}$ is a unit vector in the vertical. The bulk Richardson number relating the velocity and stability scalings is $\mathrm{Ri} = N^2\lambda_z^2/V^2 = 4\pi^2$, and $\mathbf{k} = (k, 0, m)$ is the primary GW wavenumber vector with $k = 2\pi/\lambda_x$ and $m = 2\pi/\lambda_z$. Re is as defined above and the Prandtl number is $\mathrm{Pr} = \nu/\kappa$, where κ is the thermal diffusion coefficient. The linear, inviscid dispersion relation arising from these equations for general GW orientations within the computational domain is

$$m^2 = (k^2 + l^2)(N^2/\omega^2 - 1), \qquad (4)$$

where k and l are the wavenumbers along and normal to the direction of propagation of the primary GW, respectively, $\omega = k_h c$ is the GW frequency, $k_h^2 = k^2 + l^2$, and c is the GW horizontal phase speed.

For all simulations discussed here, we assume an initial monochromatic GW having an amplitude of $a = u_0'/c = (d\theta/dz)_{\min}/(d\theta_0/dz) = 0.5$ and wavenumber in the computational domain of $(k, l, m) = (0, 0, -1)$, such that the initial GW exhibits a minimum $\mathrm{Ri} \sim 4$ in the

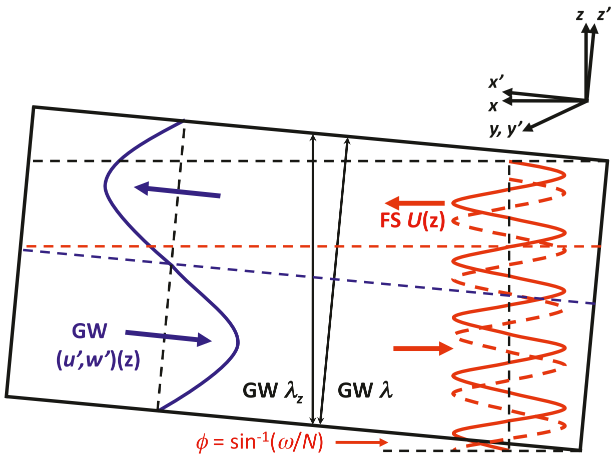

FIG. 1. Tilted computational domain aligned along the GW phase having an inclination of $\phi = \sin^{-1}(\omega/N)$ relative to horizontal. The domain and geophysical coordinates are (x', y', z') and (x, y, z), respectively; GW velocity and θ' fields are uniform along x' (blue velocity profile and dashed phase inclination); and streamwise and spanwise FS velocities are uniform along x (red velocity profile and dashed phase inclination). Case L0 has only streamwise FS (red solid velocity profile); case R has rotary FS with streamwise and spanwise velocities (red solid and dashed velocity profiles).

GW phase where $d\theta'/dz \sim 0$ and $du'/dz \sim N/2$, where, u' and θ' are the primary GW perturbation streamwise velocity and potential temperature. As in F09c, we also assume a GW intrinsic frequency $\omega = N/10 = N\sin\phi$ (where ϕ is the angle of the GW phase from horizontal; see Fig. 1), a constant mean stability N, and Re = 50 000 in order to enable instabilities and turbulence accompanying GW–FS dynamics extending to very small scales. Finally, we assume Pr = 1 so as to have comparable resolution requirements in the temperature and velocity fields.

To describe GW–FS interactions with as few complications as possible, we choose an FS motion field that will enable mutual deformation of the respective GW and FS flows—hence, an ability to approximate various aspects of observed flows—but have minimum complexity. We also note 1) that inertia–GWs (IGWs) having small λ_z and $\omega \sim f$ constitute much of the low-frequency spectrum throughout the atmosphere and 2) that local instability and turbulence events occur on time scales $\tau \ll T_f$, where $T_f = 2\pi/f$ is the inertial period (Fritts and Alexander 2003). Thus, we employ a sinusoidal FS in either a single plane or as a rotary field as an approximation to either IGW or mean motions to examine the effects of such GW–FS superpositions.

Three DNSs having FS $V(z) = (2N/m_{\mathrm{FS}})\sin(m_{\mathrm{FS}}z)$, with $V(z)$ aligned in the (streamwise) plane of GW motions, and at 45° and 90° to the streamwise plane, are denoted cases L0, L45, and L90, respectively. The three planar FS cases have maximum FS shears of $(dV/dz)_{\max} = 2N$ such that the minimum FS Ri = 1/4. The rotary FS DNS (denoted case R) employs streamwise and spanwise mean FS velocities given by $[U(z), V(z)] = (2N/m_{\mathrm{FS}})[\sin(m_{\mathrm{FS}}z), \cos(m_{\mathrm{FS}}z)]$, for which the FS Ri = 1/4 everywhere. The mean FS velocity thus rotates clockwise with height and represents the limiting case of an inertia–GW as ω approaches f in the Northern Hemisphere. Here, we specify the FS vertical wavelength to be one-fifth of the vertical projection of the end of the tilted computational domain in order to be periodic. Thus, $\lambda_{\mathrm{FS}} = \lambda_{\mathrm{GW}}\cos\phi/5$, where $\lambda_{\mathrm{GW}} = \lambda_z\cos\phi$ and λ_{GW} and λ_z are the total and vertical GW wavelengths, so that $\lambda_{\mathrm{FS}} = \lambda_z\cos^2\phi$ or $m_{\mathrm{FS}} = 2\pi/\lambda_{\mathrm{FS}} = 10\pi/(\lambda_z\cos^2\phi)$. The $\cos\phi$ factors arise because the GW is periodic in the computational domain along the GW phase direction, but FS must be periodic along the vertical projection of the tilted ends of the computational domain (see below). This FS scale differs from the GW–FS DNS described by F09c, which assumed $m_{\mathrm{FS}} = 10m_{\mathrm{GW}}/\cos^2\phi$. The larger FS scale here allows the current DNS to achieve instability and turbulence at larger scales by about 2 times (and a larger Re by 4 times) than studied by F09c.

Figure 1 shows the computational domain chosen to accommodate both the initial GW and FS motions for the four cases examined. Streamwise, spanwise, and phase-normal directions (x', y', z') are defined along the GW group velocity, normal to the plane of primary GW motions, and opposite to the (downward) GW phase velocity, respectively. This coordinate system implies components of gravity of $-g\sin\phi$ and $-g\cos\phi$ and potential temperature gradients of $\beta\sin\phi$ and $\beta\cos\phi$ in the x' and z' directions, respectively. A domain aligned along the GW phase offers several clear advantages for several purposes: the evolving primary GW structure is trivial to assess, turbulence statistics can easily be evaluated at constant GW phase, and wave–wave interactions involving GWs having much lower frequencies and/or large horizontal scales are allowed that would be impossible to describe in a horizontally confined horizontal domain. Tilted domains nevertheless impose their own allowed mode interactions, and these are different, though arguably more general, than are enabled in a horizontal domain of similar dimensions.

GW velocities (blue thick line and arrows) in Fig. 1 are parallel to the upper and lower domain boundaries; FS mean horizontal streamwise and spanwise velocities (red thick lines and arrows) are shown with solid and dashed lines, respectively. Thin dashed blue and red lines show the phase slopes of the initial GW and FS velocities, respectively. To satisfy the requirement for periodicity for both fields in the tilted domain, the streamwise dimension must be a multiple of $X' = Z'/(5\tan\phi) = 1.993Z'$, and we employ the minimum streamwise length to achieve the highest computational efficiency. The spanwise domain width is chosen to be $Y' = 0.5Z'$ to ensure an ability to define any instability structures that might arise for the cases considered. Visualization of GW, instability, and turbulence structures employs 2D cross sections of vorticity magnitude and total and perturbation potential temperature (θ and θ', respectively).

b. Computational methods and optimization

Our solution algorithm is pseudospectral and employs a Fourier series representation of the field variables in each direction, the third-order Runga–Kutta (RK3) method of Spalart et al. (1991) for time integration, a variable time step (owing to varying velocities and model resolution) with a Courant–Friedrichs–Lewy (CFL) upper limit of 0.68 to ensure numerical stability and precision, and a "two-thirds rule" spectral truncation to avoid backscatter to larger spatial scales (Werne and Fritts 1999, 2001). Incompressibility is enforced via a two-streamfunction formulation with the streamfunctions defined by the vertical velocity and vertical vorticity fields, and linear and nonlinear terms are treated implicitly and via transformation to, and multiplication in, physical space, respectively (Werne et al. 2005).

To achieve approximate isotropic resolution of instability and turbulence structures at small scales, we employ spectral resolution as high as (3456, 864, 1728) and (2560, 640, 1280) Fourier modes for cases L0 and R, respectively, based on evolving resolution needs. Initial conditions include the superposed initial GW and FS fields defined for each case. A white-noise spectrum in the initial potential temperature field having an RMS amplitude of 10^{-8} (compared to $a = 0.5$ for the GW) yields a near-inertial-range spectral shape (slope ~ -2) at wavenumbers k, l, $m \sim 20$–200 relative to the gravest streamwise wavenumber at $t \sim 4T_b$ prior to instability onset.

To take full advantage of the cache architecture of the supercomputers on which these DNSs were performed (Cray XT4 and XE6 systems at several Department of Defense (DoD) HPCMP supercomputer centers), FFTs are performed on contiguous data requiring data transposes to successively rotate the x', y', and z' directions into the first array index and a global transpose requiring all-to-all communications among processors (Julien et al. 1996).

3. GW–FS flow evolutions

a. Overview of evolutions of GW–FS fields and domain-averaged energetics and spectra

1) GW–FS PROFILES AND ENERGY EVOLUTIONS

The influences of GW–FS interactions on the overall flows for cases L0 and R are illustrated in Fig. 2 with profiles along z' of potential temperature and the three component velocities, θ, u, v, and w (in the domain reference frame), at the center of the computational domain from $t = 0$ to $24T_b$ at an interval of $2T_b$. Corresponding time series of the nondimensional GW horizontal velocity and potential temperature amplitudes, $a = u_0'/c$ and $(d\theta'/dz)/(d\theta_0/dz) = (d\theta'/dz)/\beta$, the 2D ($l = 0$) and 3D ($l \neq 0$) kinetic and potential energies (excluding the initial GW and FS), the component turbulence kinetic and potential energies, and the streamwise velocity amplitudes of the five largest 2D GWs arising because of wave–wave interactions from $t = 0$ to $25T_b$ are shown in Fig. 3.

Considering first the θ' and u' profiles shown in the top two panels of Fig. 2, we see that FS shears in both cases L0 and R quickly yield regions of reduced or negative local static stability, $N^2 = (g/\theta_0)d\theta/dz$, because of horizontal shearing of tilted isentropes accompanying the GW phase structure. Four such sites are seen at $t = 2T_b$ (second profiles), and more arise up to $t \sim 10T_b$ because of the continued FS advection and downward progression of the GW phase. The four initial sites of minimum N^2 at $t = 2T_b$ are indicated with short horizontal lines in both panels for reference. The upper three sites (two of which have $N^2 < 0$) are seen to have $du/dz' > 0$ (positive x' and u is up and to the left; see Fig. 1), while the lower site has the opposite shear. In each case, these are consistent with the tilts of the θ surfaces of the GWs, which have $d\theta'/dx' < 0$ at the upper three sites and $d\theta'/dx' > 0$ at the lower site at this time. These sites of combined high shear and small or negative N^2 intensify with time and eventually enable the development of local instabilities [the instability forms and evolutions are described in detail in sections 3b and 3c below] that lead to local turbulence and mixing quickly thereafter. This mixing at each layer largely restores the static stability to neutral values, though initial instabilities at these layers appear to occur more rapidly for case L0 (beginning at $t \sim 4.7T_b$) than for case R (beginning about $1T_b$–$2T_b$ later; see below). In each case, successive unstable layers also exhibit rapid instability, turbulence, and mixing, which yield sheet and layer structures that persist to late times.

Turning now to the temporal evolutions displayed for cases L0 and R in Fig. 3, we see that the primary GW amplitudes and the 2D potential energy evolutions are essentially identical out to $t \sim 7T_b$, after which relatively small differences arise and increase with time. In each case, GW amplitudes decline sharply (by about 30%–40%) by $t \sim 7T_b$–$10T_b$, and remain relatively constant thereafter. GW horizontal velocity and temperature oscillations are suggestive of excitation of a weaker 2D component (via wave–wave interactions) having the

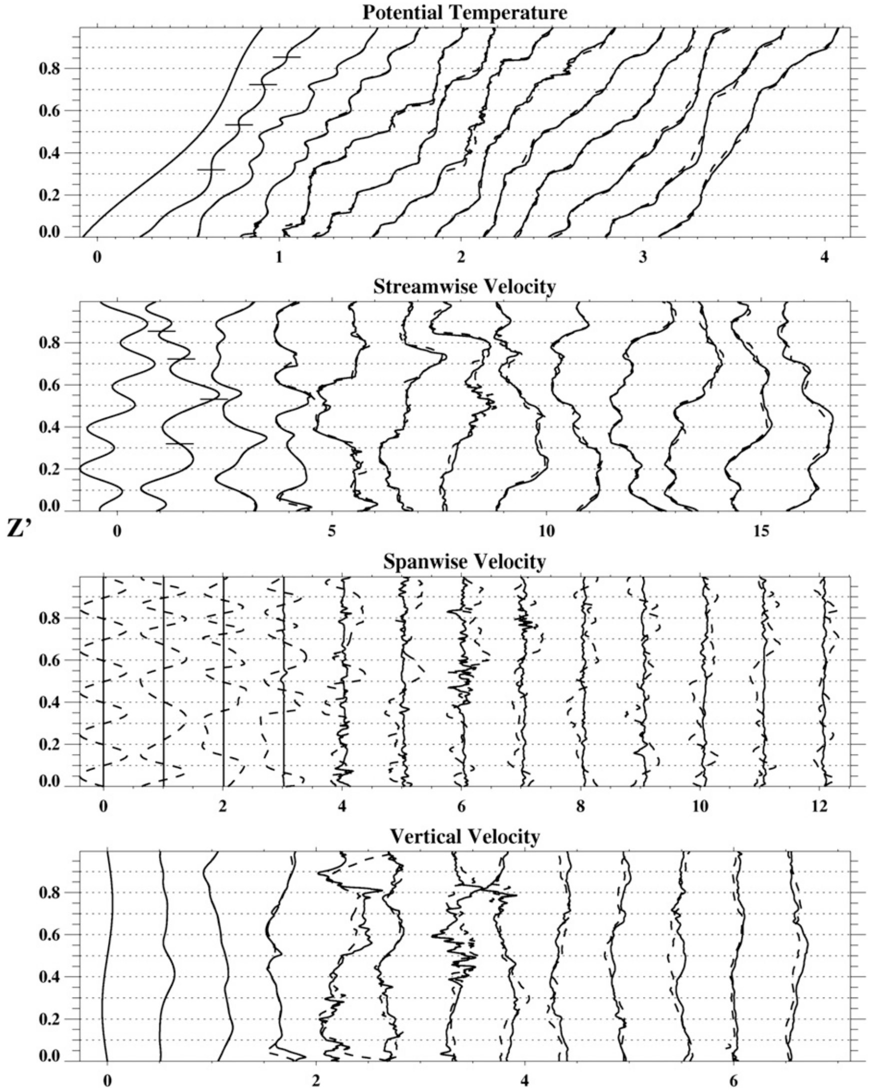

FIG. 2. Profiles along z' of (top) nondimensional θ and (second row)–(bottom) the three component velocities u, v, and w at the center of the computational domain from $t = 0$ to $24T_b$ with an interval of $2T_b$. Cases L0 and R are shown with solid and dashed lines, respectively. Offsets between adjacent profiles are 0.22, 0.7, 1.2, and 0.7 units, respectively.

same spatial structure as the initial GW, but opposite phase progression [e.g., wavenumber (0, 0, 1)] rather than that for the primary GW of (0, 0, −1). Additional evidence for this interpretation includes an apparent ''beat'' between the velocity and potential temperature fields at approximately half the GW period.

Primary GW amplitude decreases in each case cannot be attributed to instabilities and turbulence, given that these small-scale dynamics can have no influence on the 2D GW fields until $t \sim 5T_b$ and later (see the top right panels of Fig. 3). Instead, 2D ($l = 0$) kinetic and potential energy increases and the five largest 2D GW streamwise velocity amplitudes for modes having $|m'| = 1$–5 (all with $|k'| = 1$) reveal that 2D wave–wave interactions are the sole cause of the initial primary GW amplitude decreases (see Fig. 3). Specifically, no modes having $l \neq 0$ arise until 3D instabilities occur in either case. Even following 3D instabilities and turbulence, the 2D GW fields remain nearly the same in the two cases. Thus, the presence of initial spanwise velocity FS in case R has little or no influence on the evolution of the 2D GW field, but it does account for the increased 2D KE in case R relative to case L0 at early times. It is not twice the 2D KE in case L0, however, because both the initial GW and FS contribute to the 2D KE and PE arising at new wavenumbers in each case.

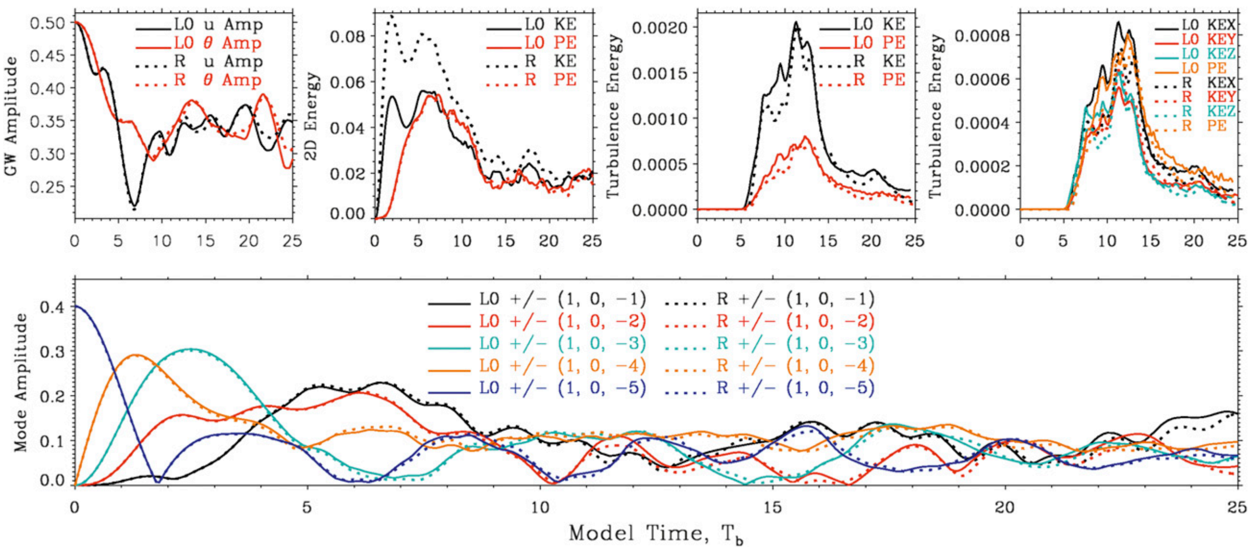

FIG. 3. (top left)–(top right) Nondimensional primary GW streamwise velocity and θ amplitudes, 2D ($l = 0$) kinetic and potential energies, 3D ($l \neq 0$) total velocity and temperature variances, and 3D component velocity and temperature variances. Cases L0 and R are shown with solid and dashed lines, respectively, in all panels. GW velocity amplitudes and variances are shown with black lines and GW velocity θ amplitudes and variances are shown with red lines, respectively, in the left three top panels. Component kinetic and potential energy line codes are shown in the top right panel. (bottom) Amplitudes of the streamwise FS and the gravest GW modes arising from wave–wave interactions, with line codes as shown.

Referring to the GW amplitude evolutions in Fig. 3, we see that the new GW modes arise in a specific sequence. Denoting the wavenumber for a specific GW as $\mathbf{k}'_i = (k'_i, 0, m'_i)$ and those for the initial GW and FS as $\mathbf{k}'_{\rm GW} = (0, 0, -1)$ and $\mathbf{k}'_{\rm FS} = (1, 0, -5)$, the first GW to arise from wave–wave interactions (orange lines in the bottom panel of Fig. 3) has a wavenumber

$$\begin{aligned}\mathbf{k}'_1 = (1, 0, m'_1) &= \mathbf{k}'_{\rm FS} - \mathbf{k}'_{\rm GW}\\ &= (1, 0, -5) - (0, 0, -1) = (1, 0, -4)\end{aligned} \tag{5}$$

and successive GWs have wavenumbers

$$\begin{aligned}\mathbf{k}'_i = (1, 0, m'_i) &= \mathbf{k}'_{i-1} - \mathbf{k}'_{\rm GW}\\ &= (1, 0, m'_{i-1}) - (0, 0, -1) = (1, 0, m'_{i-1} + 1).\end{aligned} \tag{6}$$

Thus, in each case wavenumber $\mathbf{k}'_{i-1}$ precedes $\mathbf{k}'_i$, at least up to GW wavenumber $\mathbf{k}'_4 = (1, 0, -1)$. The overall result is excitation of additional GWs typically having lower rather than higher frequencies compared to the initial GW.

The evolutions of the 3D fields in cases L0 and R differ more significantly than the 2D evolutions. Local instabilities and turbulence in case L0 can only arise because of 2D shears and temperature gradients in the streamwise vertical (hereafter streamwise) plane. In case R, FS shears in both the streamwise and spanwise directions are able to contribute to local instabilities. Interestingly, however, instabilities and turbulence are delayed in case R relative to case L0, despite the additional spanwise shear source for turbulence kinetic energy, the doubled FS shear variance, and the potential for additional instability modes and orientations.

Three-dimensional ($l' \neq 0$) kinetic and potential energies in case L0 [assumed to be largely turbulence energies, turbulent kinetic energy (TKE) and total potential energy (TPE), respectively, following initial instability dynamics] begin to increase strongly just after $t = 5T_b$, with TKE exhibiting the largest response and achieving an initial maximum at $t \sim 7.5T_b$ and successive larger maxima extending to $t \sim 12.5T_b$ (see section 3b below). TPE increases accompany those for TKE but are about 3–4 times smaller than TKE at early stages. The top right panel of Fig. 3 indicates that contributions to TKE by the three 3D velocity components vary significantly, with the spanwise component about 25% smaller throughout the evolution, but the vertical component decreasing to comparable values following strong initial instability. This can be understood by examining the character of the initial instabilities in case L0, which yield primarily vertical fluid displacements relative to the local GW–FS flow (see section 3b). This results in primarily streamwise and vertical velocity perturbations because of the strong streamwise FS shears at these locations and times (see Fig. 2, top, and section 3b). As more general instabilities arise, spanwise and vertical components remain smaller than the streamwise component (by 30%–50%). TPE becomes competitive with,

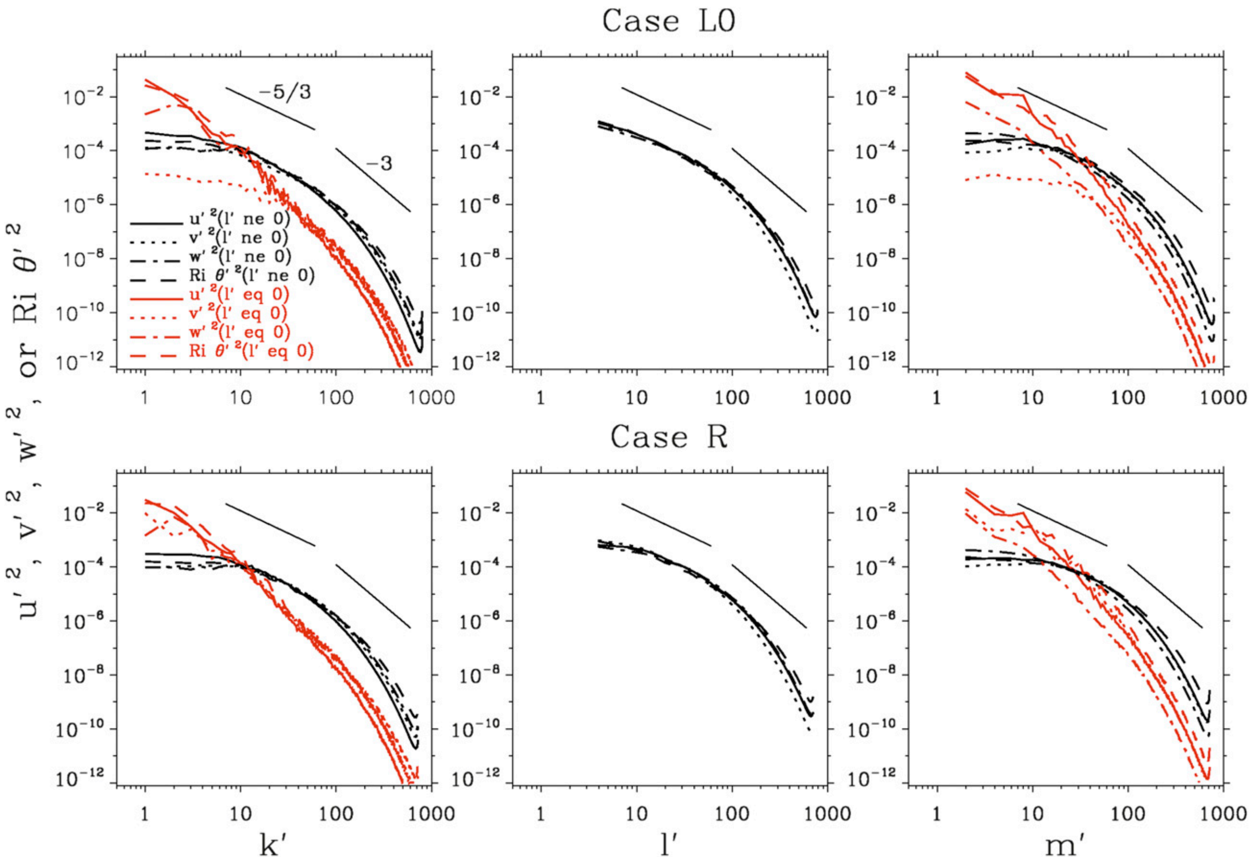

FIG. 4. Domain-averaged component variance spectra of u', v', w', and Ri θ' vs (left) k', (middle) l', and (right) m' for cases (top) L0 and (bottom) R at $t = 11.5T_b$. The 2D ($l' = 0$) and 3D ($l' \neq 0$) spectra are shown with red and black lines, respectively. (top left) Line codes are shown. Also shown in each panel are spectral slopes of $-5/3$ and -3 for reference.

or larger than, the streamwise TKE component throughout their strong decay beginning at $t \sim 12T_b$ and extending to late times. Individual instability events continue to occur at later times because of successive GW–FS superpositions, but these become weaker and less frequent with time. TKE and TPE exhibit final, weaker maxima accompanying such an event extending from $t \sim 17T_b$ to $21T_b$.

TKE and TPE evolutions in case R closely parallel those in case L0, but with initial TKE and TPE growth delayed by about $1T_b$ or less. This similarity is apparently a result of similar, strong instability dynamics accompanying the initial overturning (see discussion of Fig. 5 at $t = 5T_b$ below) despite the earlier occurrence of initial instabilities in case L0. Case R TKE and TPE remain about 30% less than for case L0 throughout the evolutions, except during the strongest decay phase, where they are competitive or larger. This suggests delayed TKE and TPE generation relative to case L0 accompanying the greater 2D FS KE in case R (second top panel in Fig. 3). It is surprising, however, that case R TKE and TPE are generally smaller than those for case L0, given the larger 2D FS sources extending to late times.

Compared to cases L0 and R, case L45 displays wave–wave interactions in the streamwise plane, but these evolve significantly more slowly than in case L0 because the FS amplitude in case L45 in the streamwise plane is smaller by $2^{1/2}$. Instabilities and turbulence do occur in case L45, but these arise much later and with much smaller energies than in case L0. Case L90 exhibits only weak wave–wave interactions and no local instability or 3D structure out to $t = 60T_b$. As a result, neither case L45 nor case L90 will be discussed further.

2) VARIANCE SPECTRA

Variance spectra for cases L0 and R are shown in the top and bottom panels, respectively, of Fig. 4 at $t = 11.5T_b$, at which the two DNSs have reached comparable stages in their instability and turbulence evolutions. Black and red spectra in each case are for motions having $l \neq 0$ and $l = 0$, respectively. Note also that variances are computed in the frame of the computational domain. Both cases exhibit about 1–2-decades-higher 2D ($l = 0$) than 3D ($l \neq 0$) u' and θ' variances at $k' \leq 5$ and $m' \leq 10$, suggesting dominance by 2D GW motions at larger streamwise and vertical scales at this time. Two-dimensional w' variances are also larger at small k' and m', but by smaller amounts at small k'. The 2D spanwise velocity variance is also significantly smaller in case L0 at k' and $m' \sim 20$ and less, further confirming the essentially 2D (streamwise) orientation of the large-scale flow. The velocity variances in both cases are consistent with the largest-amplitude secondary GWs arising because of wave–wave interactions, which have phase slopes and frequencies comparable to or lower than the initial GW, thus much smaller vertical than streamwise velocity variances (see Fig. 3). The 2D streamwise and vertical velocity variances and the temperature variances in both cases fall below their 3D counterparts at $k' \sim 10$ and $m' \sim 10$–30, above which both motion fields are dominated by small-scale turbulence. Crossover wavenumbers for case L0 are also slightly smaller for both k' and m' spectra.

Three-dimensional turbulence spectra in the two cases exhibit several clear similarities. All show a well-developed inertial range extending over a decade or more above the 2D to 3D crossover wavenumbers. Temperature variances are somewhat larger than the component velocity variances in both cases at larger k', l', and m', but systematically smaller than the total velocity variances throughout the inertial range. Streamwise spectra of streamwise velocities and vertical spectra of vertical velocities are smallest at the highest wavenumbers in both cases.

b. Case L0: Aligned GW and FS velocities

The evolution of local instability and turbulence structures for case L0 (having only initial streamwise GW and FS velocities) is illustrated with streamwise- and spanwise-vertical (hereafter spanwise) cross sections of vorticity magnitude through the center of the computational domain from the initial stages of instability to $t = 13T_b$ ($1.3T_{\mathrm{GW}}$), beyond which sources of instability and turbulence energies are weaker because of earlier GW amplitude and FS shear and amplitude reductions. Streamwise cross sections are shown in the left panels of Figs. 5 and 6, with the initial evolution displayed at a $1T_b$ interval (to $10T_b$) and the more turbulent phase approaching the second maximum displayed at a 0.5-T_b interval to $t = 13T_b$. Figure 7 shows the same fields from $t = 18T_b$ to $20.5T_b$ in the upper half of the computational domain, which exhibit another instability and turbulence event that emphasizes the universal behavior of these events. Spanwise cross sections are shown at various times in Fig. 8 from $t = 5.5T_b$ to $12T_b$ to help define the initial 2D or 3D character of the instability structures. Implications of these dynamics for the total and perturbation θ fields are illustrated in Fig. 9 and discussed with respect to the corresponding vorticity fields below.

Several distinct types of instabilities are seen to occur at various stages of the L0 DNS, all of which have close analogs in other flows that are common in sheared and stratified fluids. One is an extension of the classical KHI occurring in plane-parallel shear flows or flows distorted by GWs, a second comprises counterrotating streamwise vortices deriving TKE and TPE from a combination of strong shears and regions with $N^2 < 0$, and a third bears a close resemblance to GW breaking in more idealized flows. Local KHI in the plane of GW propagation is seen to occur at smaller scales on a number of the thin vorticity sheets from $t = 6T_b$ to $13T_b$ in Figs. 5 and 6. Larger-scale KH billows arise less frequently on deeper vorticity sheets that intensify owing to GW–FS superpositions. Examples of these larger billows that quickly become turbulent are seen to arise at both ends of the extended, nearly horizontal vorticity sheet seen in the upper portion of the domain from $t \sim 10.5T_b$ to $12.5T_b$.

Referring to the spanwise cross sections of vorticity magnitude in Fig. 8, we see a predominant instability character at early times (to $t \sim 6T_b$) that closely resembles that seen as a secondary instability in the outer portions of KH billows occurring for small Ri and large Re (Klaassen and Peltier 1985; Thorpe 1987; Palmer et al. 1996; Fritts et al. 2003, 2012; Werne et al. 2005). These instabilities comprise counterrotating streamwise-aligned vortices (having high spanwise wavenumbers). Inspection of Fig. 2 and the top panels in Fig. 5 reveals that these instabilities typically occur at every other vorticity sheet in regions where the GW shear du'/dz has the same sign (see the discussion of Fig. 2 above). This can be traced to the superposition of the GW and FS shears: instability is favored at the FS vorticity sheets that are enhanced by GW vorticity of the same sign and that exhibit formation of layers having small or negative N^2 owing to FS advection of the GW potential temperature field. As these initial instabilities attain finite amplitudes, strong self- and mutual interactions quickly drive 3D vorticity dynamics and cascade enstrophy to smaller scales (Arendt et al. 1997, 1998; Andreassen et al. 1998; Fritts et al. 1998). Successive occurrences of this instability are also seen at later times at sites exhibiting the same initial advection dynamics that have not yet experienced instability (see Fig. 8 at $t = 7T_b$ and after). But they become increasingly distorted with time at even the initial stages because of the increasing complexity of the environments in which they arise.

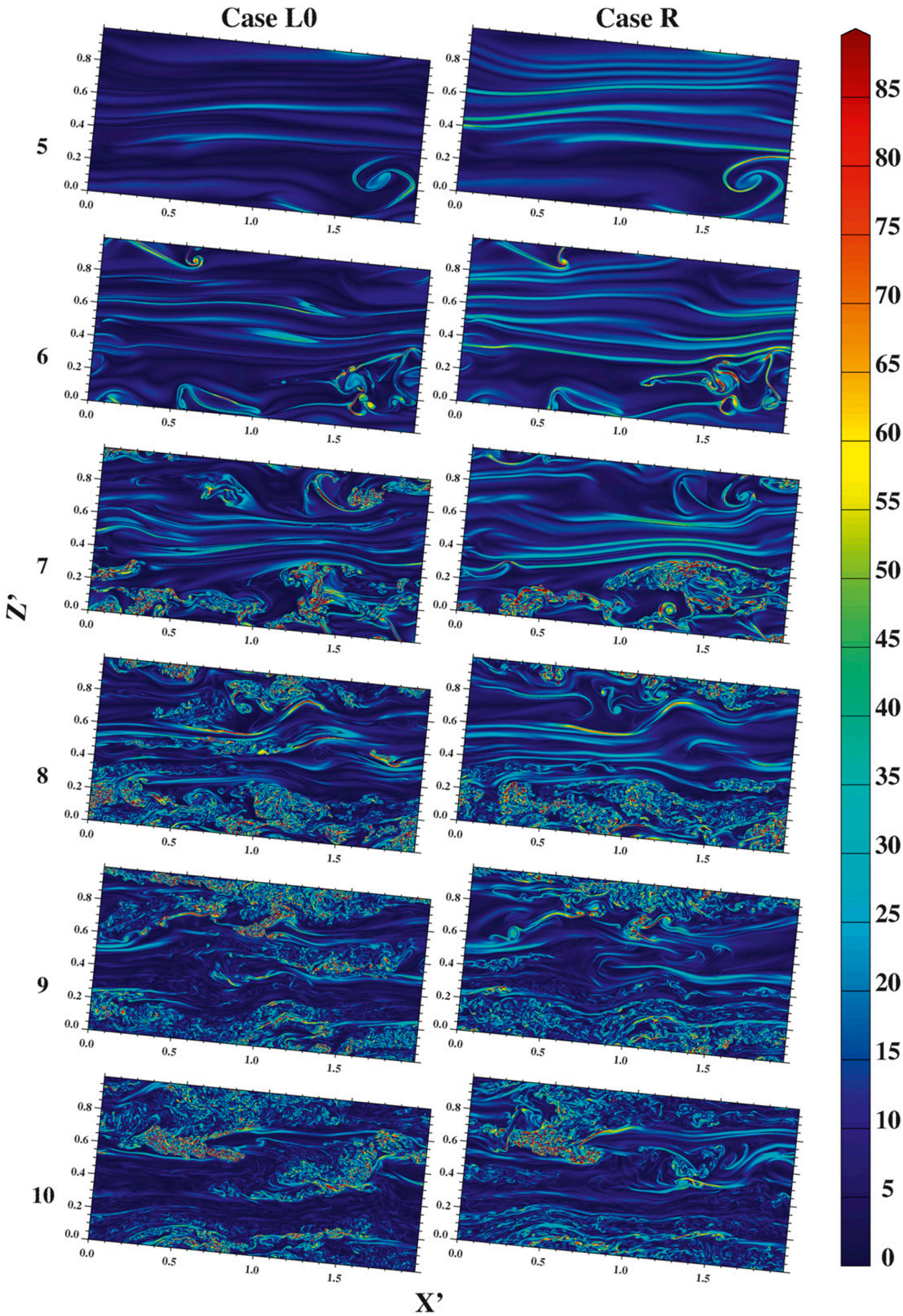

FIG. 5. Streamwise vertical cross sections of vorticity magnitude at the center of the computational domain at (top)–(bottom) $t = 5, 6, 7, 8, 9$, and $10T_b$ for cases (left) L0 and (right) R. Note the different instability and turbulence character in case R compared to case L0.

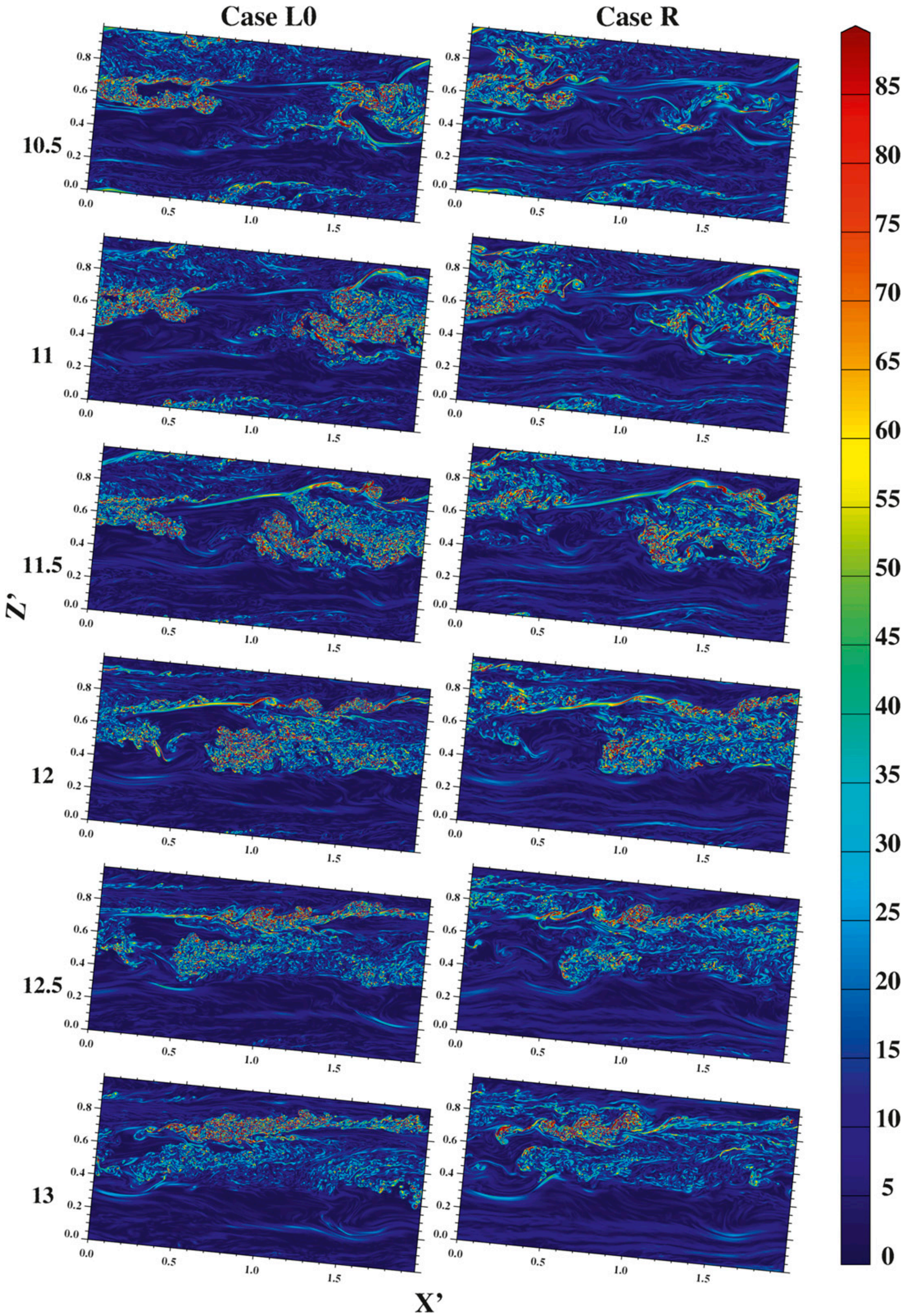

FIG. 6. As in Fig. 5, but for t = 10.5, 11, 11.5, 12, 12.5, and $13T_b$.

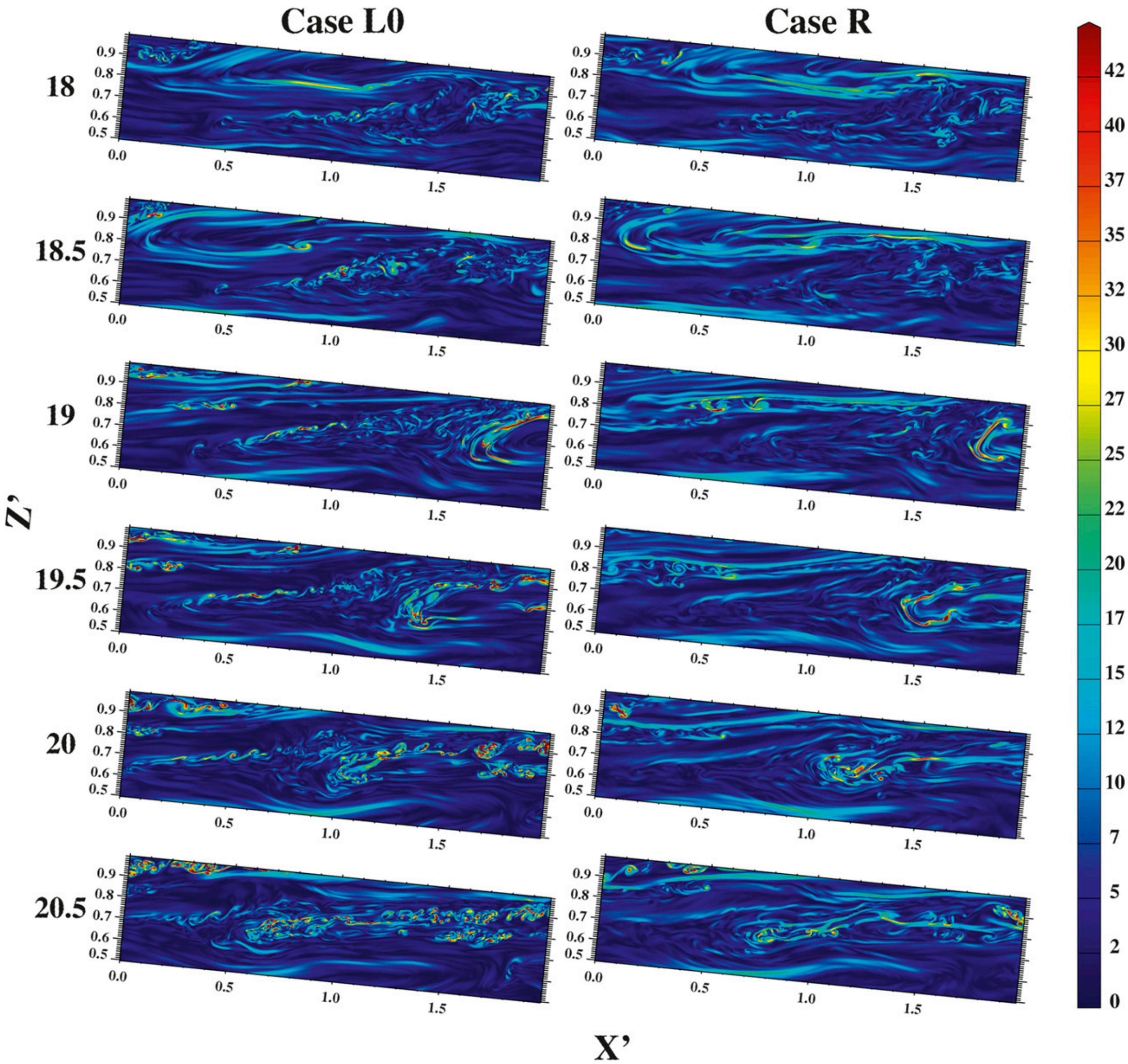

FIG. 7. As in Fig. 5, but for the upper half of the computational domain at $t = 18, 18.5, 19, 19.5, 20$, and $20.5T_b$. Note the smaller range of the color scale relative to Figs. 5 and 6.

Small-scale KHI is seen at numerous locations and times throughout the case L0 evolution, often at very small scales on intense, local vorticity sheets. Examples include 1) small KH billows at center right at $t = 9T_b$, 2) lower and middle center right at $t = 10T_b$, 3) lower center right and upper left at $t = 10.5T_b$, and 4) upper left and center at $t = 12.5T_b$. Larger-scale KHI is less frequent but is prominent, and strongly turbulent, when it occurs. The clearest example occurs on the strong, nearly horizontal vorticity sheet seen in the upper approximately one-third of the domain and intensifying from right to left from $t = 10.5T_b$ to $12.5T_b$ in Fig. 6 (left).

A third instability type seen at earlier and later stages of the L0 DNS exhibits overturning and/or fluid ''intrusions'' closely resembling GW breaking at amplitudes above and below $a = 1$ (Fritts et al. 2009a,b). That seen in the lower-right portion of the domain at $t = 5T_b$ in Fig. 5 (left) occurs at a large vertical scale. This is because it accompanies the least statically stable and upward GW phase, which is preceded by GW deformation of the FS (horizontal convergence at this altitude) that significantly expands the FS-layer depth and reduces its horizontal extent at this location and time. Streamwise vertical cross sections at other spanwise

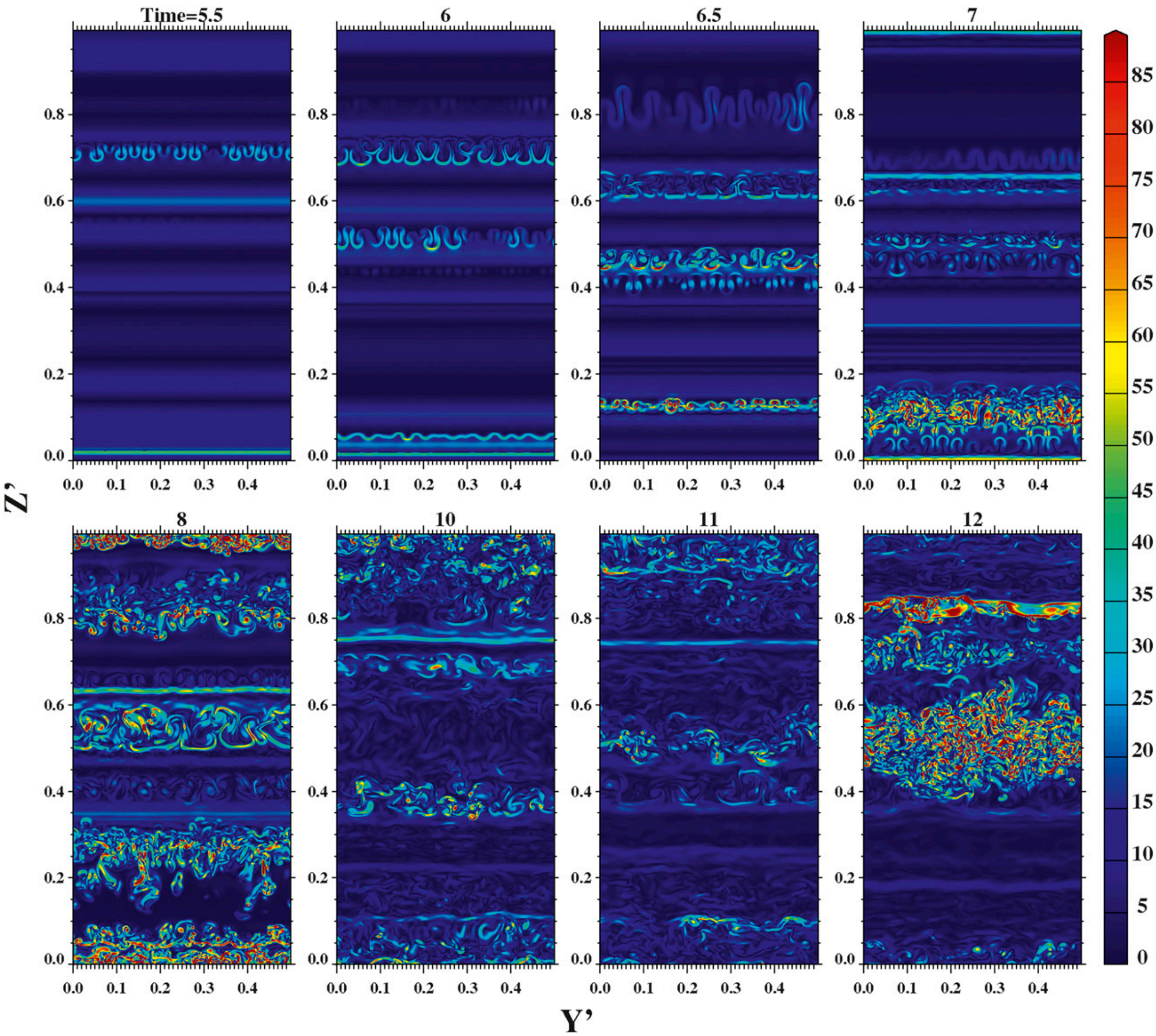

FIG. 8. Spanwise vertical cross sections of vorticity magnitude at the center of the computational domain at t = 5.5, 6, 6.5, 7, 8, 10, 11, and $12T_b$ for case L0. Note the relatively symmetric instability character at early times.

locations (not shown) reveal that this is essentially a 2D instability at $t = 5T_b$ but exhibits initial 3D structures beginning at $t \sim 6T_b$ (see Fig. 8). As seen with the KHI, however, these events rapidly become more complex with time.

We now examine in greater detail the dynamics leading to the instability types noted above. The image at $t = 5T_b$ in Fig. 5 reveals largely 2D instability dynamics until the initial 3D shear instabilities seen at $t = 5.5T_b$ in Fig. 8. These 3D instabilities have small or rightward (streamwise) advection velocities and lead to rapid generation of turbulence that is confined to relatively small layer depths in the initial turbulence transitions. As noted above, successive shear instabilities having this same form occur for significant times thereafter, although with increasing complexity due to the increasing large-scale variability.

The deeper overturning event in the lower portion of the domain at $t = 5T_b$ in Fig. 5, accompanying a layer having rapid motion in the direction of GW propagation (upward and leftward in Fig. 5 and rightward in the second row of Fig. 2), is initially 2D and laminar but becomes 3D at $t \sim 6T_b$ (see Fig. 8) and strongly turbulent within about $1T_b$–$2T_b$ thereafter. A more rapidly advecting portion of this same layer leads the overturning event by about 0.5 of the streamwise domain and evolves into an intrusion yielding a horizontally extended turbulence layer (see the upper portion of the domain from $t = 6T_b$ to $10T_b$ in Fig. 5). The

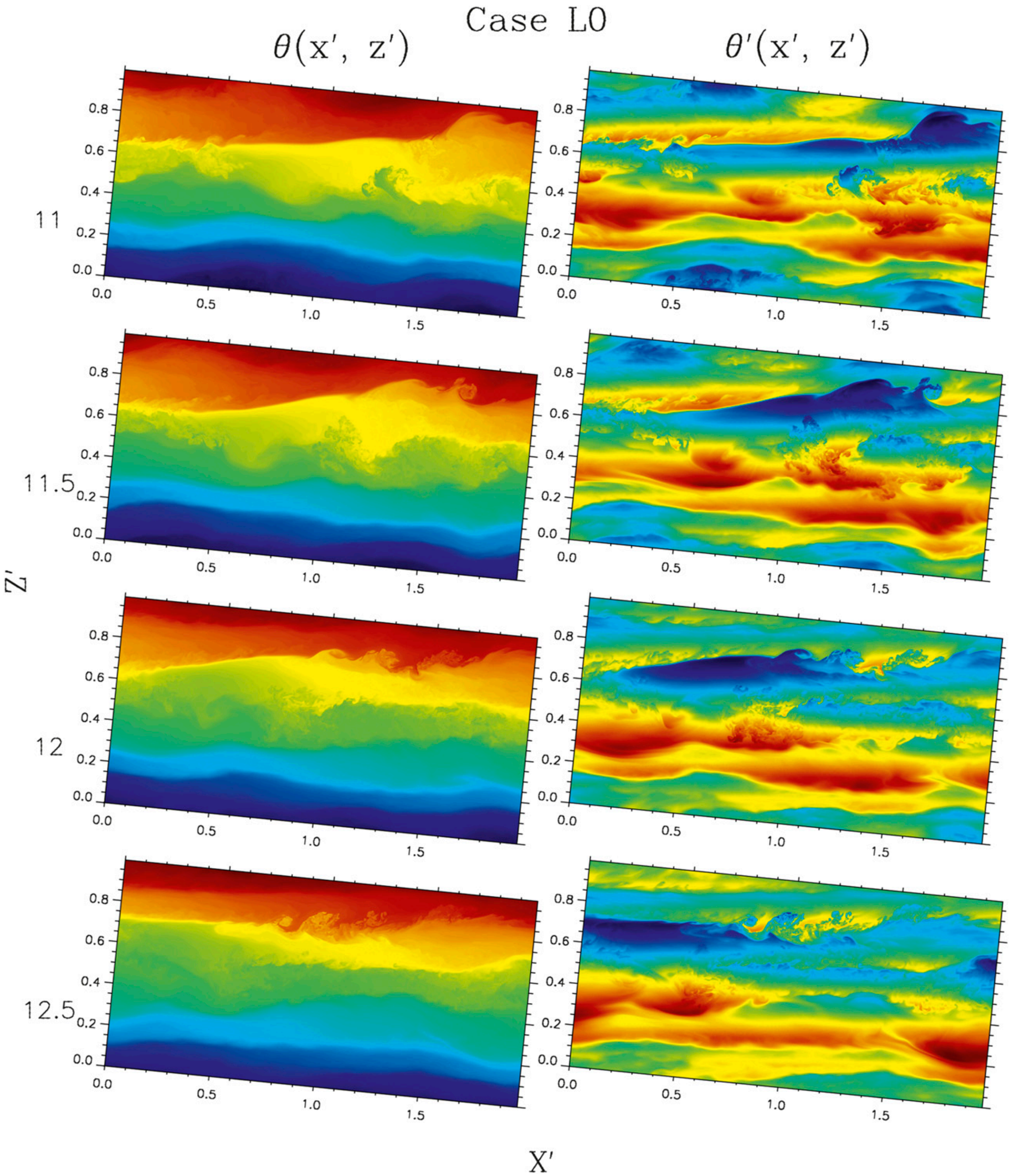

FIG. 9. As in Fig. 5, but for (left) θ and (right) θ' for case L0 at $t = 11, 11.5, 12$, and $12.5T_b$. Color scales ranging from coldest (deep blue) to hottest (deep red) span the maximum range in each case.

maximum velocity of this feature is $u' \sim 0.7$ (a dimensional velocity of approximately $0.7\lambda_z/T_b \approx 0.7c$).

These dynamics are followed by several layers of leftward motions confined largely to the region in which the GW motion is leftward in Figs. 6 and 7 (centered at $z' \sim 0.8$ at $t = 9T_b$ and descending to $z' \sim 0.5$ at $t = 12.5T_b$). Two layers have especially rapid leftward motions from $t \sim 9T_b$ to $10T_b$. One layer occurs at $z' \sim 0.8$ and $x' \sim 1$–1.5

at $t = 9T_b$ and exhibits a distinct tilted vorticity sheet, has a velocity $u' \sim 1$ and descends to $z' \sim 0.6$–0.7 by $t = 10T_b$. A second layer is centered at $z' \sim 0$ at $t = 9T_b$, also exhibits a distorted, but less distinct, vorticity sheet and achieves a $u' \sim 0.9$. Their subsequent evolutions and instabilities are very differently, however.

The upper layer encounters weak or opposite motions ($u' < 0$) from $t \sim 9T_b$ to $10T_b$ that induce localized and small-scale KHI above and below (see Fig. 5 at $t = 10T_b$). This flow continues to penetrate leftward and evolves into a long, turbulent intrusion, merging with another descending plume between $t \sim 11T_b$ and $12T_b$, and extending across the center of the domain at the last times displayed in Fig. 6. The second layer at $z' \sim 0$ at $t = 9T_b$ identified above exhibits a less coherent vorticity sheet with KHI occurring at several scales, stalls (with $u' \sim 0.2$), and largely abates by $t \sim 10.5T_b$. Thereafter, however, this same vorticity sheet, although advecting leftward very slowly, intensifies again owing to the quasi-2D GW field. This results in large-scale, turbulent KHI that progresses leftward following the intensifying vorticity sheet that is distinct from, but coincident with, the later stages of the intrusion at lower levels. The dominant KH billows arising between $t \sim 11T_b$ and $12T_b$ suggest a small initial Ri due to their depth and vigorous secondary instability, turbulence, and mixing.

Subsequent intrusions do not exhibit strong overturning (owing to the early GW amplitude reduction), but they all exhibit a strong surge of leftward motion (along the FS in the direction of the GW group velocity, with u' approaching 1) where the GW and FS velocities superpose constructively. Several (not shown) accompany strong flows extending from $t = 12T_b$ to $16T_b$ at middle and lower levels seen in Fig. 2. Another significant intrusion is seen to occur beginning at $t \sim 18T_b$ with $u' \sim 1$ and to penetrate in the direction of GW propagation until $t \sim 20.5T_b$ (see Fig. 7), though turbulence intensities appear significantly smaller in this case. Several intrusions at the center of the streamwise domain seen in Fig. 2 exhibit quite sharp maxima.

The correlations of these turbulent intrusions with flows having $u' \sim 1$ suggest an analog with GW breaking (where $a = 1$ implies $u' = c$) in which the amplitude of the superposed flow (measured relative to the GW phase speed) is sufficient for local instability. This suggests an "intrusion" velocity due to the superposition of a dominant GW and local FS that exceeds, or is comparable to, the GW phase speed may be a good predictor for turbulence generation, expressed as

$$u'_{\text{int}} \sim c = N\lambda_z/2\pi = \lambda_z/T_b\,, \tag{7}$$

where λ_z refers to the large-scale GW.

Not all intrusion events generate strong turbulence or occur in an environment that enables them to persist over several T_b, however. Those highlighted in the discussion above and displayed in Figs. 5–7 are the strongest and most obvious at earlier times, but weaker intrusions are also seen to occur intermittently to much later times, at least as late as $t \sim 35T_b$ (not shown). Collectively, they are sufficiently distinct and frequent features of this flow that they make significant contributions to the overall turbulence statistics. As a result, we anticipate that such features of GW–FS superpositions are likely significant contributors to SBL dynamics and turbulence statistics wherever such superpositions arise.

The evolution and influences of these dynamics from $t = 11T_b$ to $12.5T_b$ in the θ and θ' fields are illustrated in Fig. 9. The θ' fields reveal both strong layering in the vertical accompanying the FS more clearly than seen in the vorticity fields. They also exhibit clear oscillatory features in the streamwise direction (streamwise wavenumbers $k' \sim 2$–4 relative to the streamwise domain) having vertical phase variations indicative of smaller-scale GWs propagating vertically.

Both θ and θ' fields emphasize that the larger-scale KHI arising during this interval evolves on a vorticity sheet initially having very high local stratification and occurring at the highest excursion of this vorticity sheet in the vertical. The KH billows that arise are seen to mix the vorticity sheet and corresponding high stratification as the KH billow train progresses from right to left. In contrast, the region of most negative θ' below the large-scale KH billows (see top right panels of Fig. 9) accompanies the strong turbulent intrusion and the upward fluid displacement that accounts for the intensification of the vorticity sheet and the resulting KHI in this region at these times. As noted in the discussion of the vorticity fields, the leading edge of this cold intrusion is itself strongly turbulent, independent of the induced KHI. The strong initial and subsequent motion of this cold intrusion in the direction of GW propagation (to the left) is thus the driver for both the KHI above and the "GW breaking" below this layer throughout its evolution.

c. *Case R: GW and rotary FS*

The evolution of instability and turbulence structures for case R (having a streamwise initial GW and a rotary FS velocity field) is illustrated with streamwise cross sections of vorticity magnitude in the right panels of Figs. 5–7 at the same times as shown for case L0 at left. As seen in Fig. 3, these times span the increase of 3D TKE and TPE from approximately zero to their maxima at $t \sim 12T_b$–$13T_b$. Spanwise cross sections of vorticity magnitude spanning the strong increases seen in the case R 3D TKE and TPE are shown in Fig. 10 at the

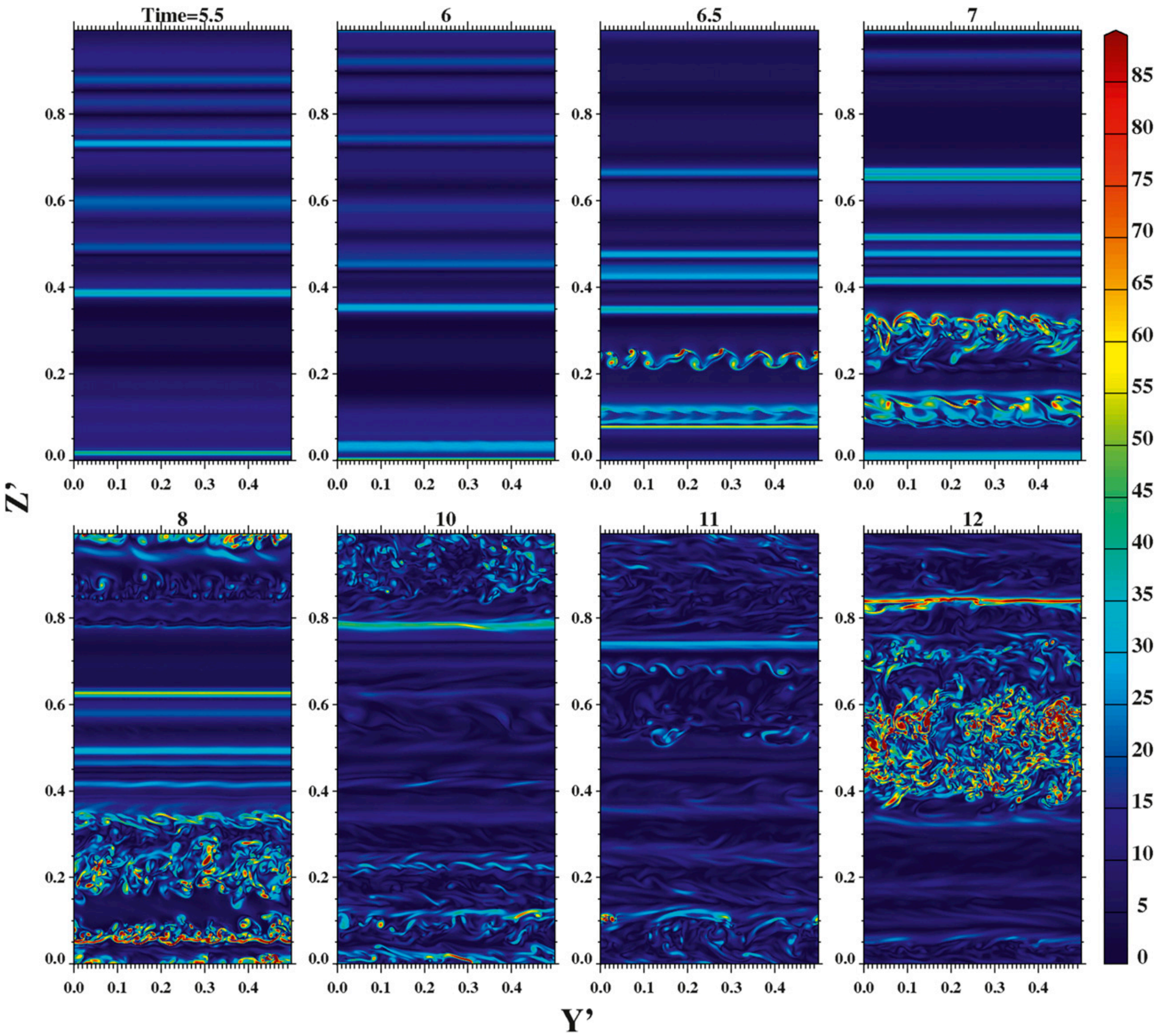

FIG. 10. As in Fig. 8, but for case R. Note the highly asymmetric instability character due to spanwise shears in case R.

same times displayed for case L0 in Fig. 8 and at higher temporal resolution in a subdomain from $z' = 0.05$ to 0.3 in Fig. 11.

As seen in case L0, the case R DNS exhibits both shear and overturning instabilities. Here, however, instability structures are strongly influenced by the spanwise FS shear at all stages. The first instabilities to arise in case L0 are the instabilities composed of streamwise-aligned counterrotating vortices in the center and upper portions of the domain (Fig. 8, top left) from $t \sim 5.5T_b$ to 6.5 T_b. But the addition of spanwise FS shear suppresses these instabilities entirely at these locations and times (Fig. 10, top left). When instabilities of the vorticity sheets do occur in case R, the character is strongly modified by spanwise shears, which enhance (weaken) those vortices with the same (opposite) streamwise vorticity (see below). The result is an asymmetric initial instability field with 3D transitions exhibiting greater spatial intermittency.

Unlike the initial counterrotating streamwise-aligned instabilities in case L0, initial overturning at the lower right at $t = 5T_b$ is common to cases L0 and R. Like the initial instabilities in case L0, spanwise shears are seen to also influence 3D instabilities accompanying this overturning in case R. Comparisons of the left and right panels in Fig. 5 at $t = 6T_b$ and of Figs. 8 and 10 at $t = 6.5T_b$ reveal that initial 3D instabilities in case R accompany the overturning dynamics rather than the quasi-horizontal vorticity sheets that were first to exhibit instability in case L0. The delay of the transition to turbulence in case R does not appear to influence the

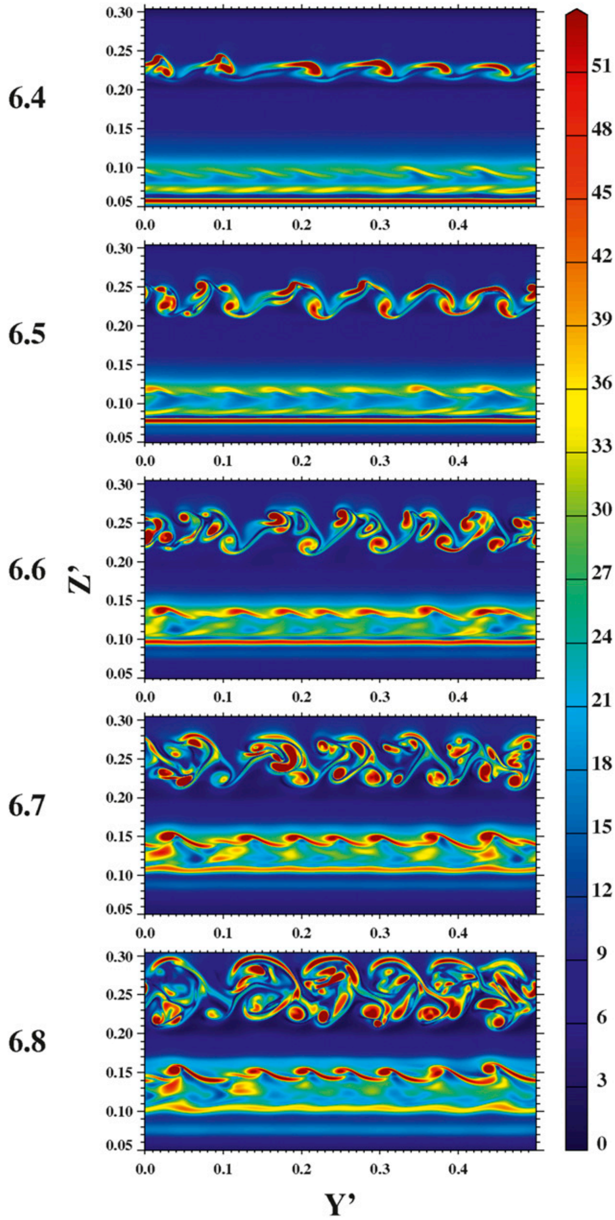

FIG. 11. As in Fig. 10, but for case R in the lower portion of the computational domain ($z' = 0.05$–0.3) at $t = 6.4$, 6.5, 6.6, 6.7, and $6.8T_b$.

occurrence of comparable turbulence scales and intensities in the overturning region and its successive evolution in each case, however. Both cases exhibit significant localized KHI in the streamwise cross sections at smaller scales at which the KH billows are typically laminar, owing to small Re, though frequently 3D owing to larger-scale flow influences.

During these instabilities and at later times, cases L0 and R exhibit very similar large-scale evolutions, including similar intrusions. These results suggest that it is the GW and FS superposition, and the associated wave–wave interactions, that primarily dictate the large-scale flow morphology and the potential for instabilities and turbulence at smaller scales.

We now examine the character of the instabilities that account for the differences in the turbulence transitions in cases L0 and R. Given the strong similarities in the larger-scale evolutions in the two cases, we expect spanwise FS shears to modulate instability structures and turbulence intensities, but not to induce strong instabilities and turbulence themselves that significantly influence the larger-scale flow.

Figure 10 displays spanwise cross sections of vorticity magnitude for case R for the same times shown for case L0 in Fig. 8. Comparing these images reveals strong influences of spanwise FS shears on instability structures throughout these time series. Most 3D instability events at early times (prior to $t \sim 8T_b$) in both cases appear to be induced by streamwise-aligned (shear aligned, spanwise wavenumber) instabilities comprising counter-rotating vortices on high-vorticity sheets. Those in Fig. 8 exhibit spanwise variations in instability structure that are largely isotropic and without any clear orientation. The cross sections in Fig. 10, however, exhibit strong anisotropies and shear influences at earlier and later times. We noted above that spanwise shear strengthened (weakened) streamwise vortices of the same (opposite) sign, and this is seen clearly in Fig. 10 at $t = 6.5T_b$. As this instability evolves, it deepens and the upper and lower portions are influenced by spanwise shears of opposite sign thereafter. Depending on their proximity, vortices in regions of opposite spanwise shear may or may not interact strongly as they evolve toward local 3D turbulence. Also seen in Fig. 10 from $t = 6.5T_b$ to $11T_b$ are small-scale KHI arising on intensified streamwise vorticity sheets. As in case L0, however, initial instabilities at later times become increasingly complex and difficult to diagnose clearly, because of the 3D large-scale environment within which they evolve.

The evolution of the shear instabilities seen to arise at the earliest time in Fig. 10 are shown with greater temporal resolution from $t = 6.4T_b$ to $6.8T_b$ in Fig. 11. These images emphasize the strong influences of opposite spanwise shears above and below the upper vorticity sheet on streamwise vortices having counter-rotating character. The dynamics are different at lower levels, where we see a streamwise vorticity sheet (with spanwise shear) exhibiting a smaller-scale KHI that evolves more slowly.

The θ and θ' fields for case R corresponding to those shown for case L0 in Fig. 9 are displayed in Fig. 12. The larger-scale features are nearly identical in each case because of the control of the larger-scale environment by 2D wave–wave interactions, which are also nearly

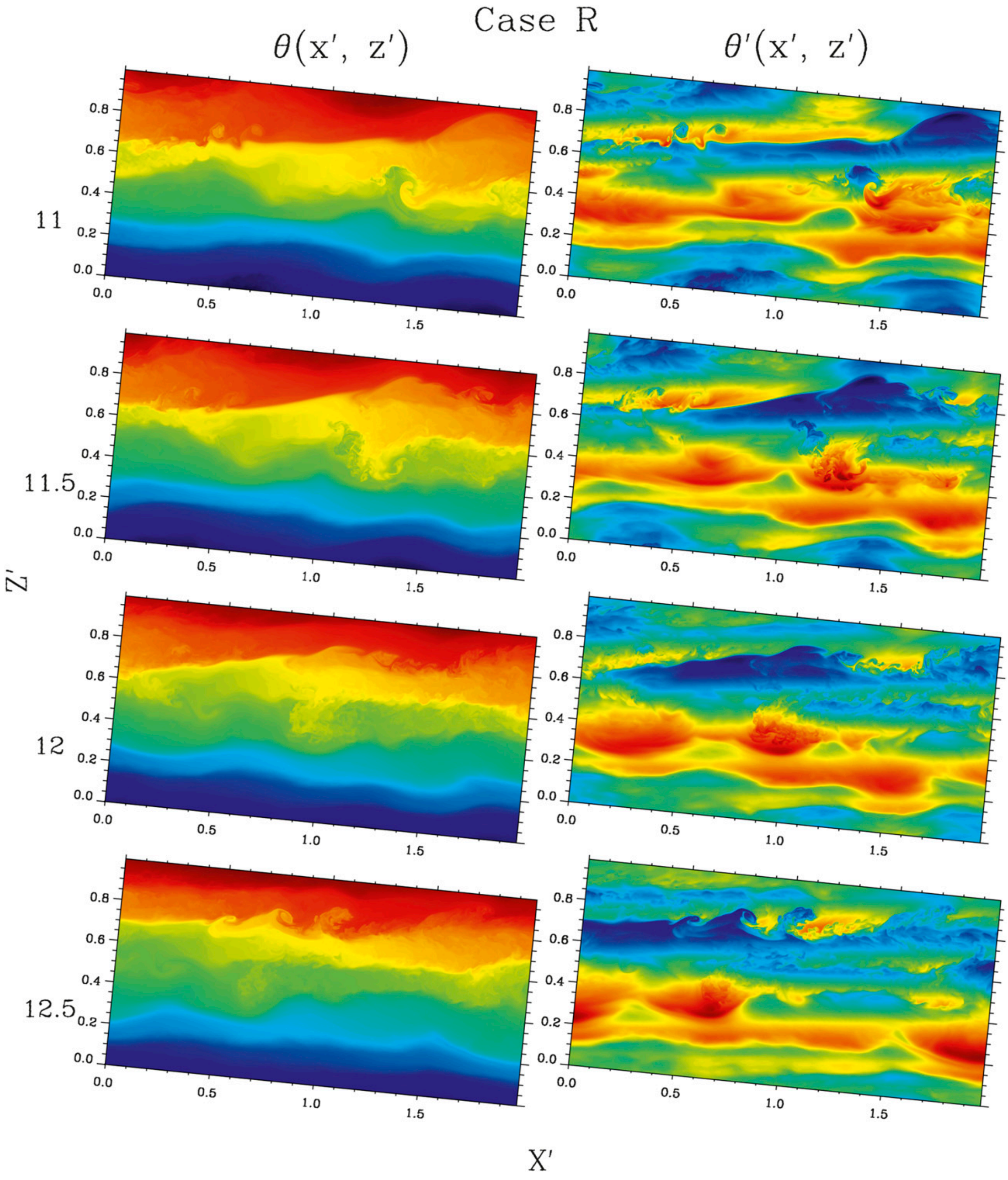

FIG. 12. As in Fig. 9, but for case R.

identical in the two cases. There are, nevertheless, clear differences in the instability and turbulence structures that reflect the differing instability onsets and subsequent turbulence evolutions in the two cases. Examples seen clearly in the θ and θ' fields include the KHI signatures, which appear more coherent in case L0 at earlier times and in case R at later times, and the character of the intrusions seen immediately below the KHI in the θ fields at $t \sim 11T_b$ and $11.5T_b$ (as discussed above for the corresponding vorticity fields in Fig. 6).

4. Discussion

Our idealized DNS of GW–FS interactions yield significant insights into multiscale dynamics in the atmosphere and oceans in several areas. These include the following:

1) energy transfers due to 2D off-resonant interactions among strictly periodic motions,
2) the character of instabilities and sources of turbulence in multiscale flows,
3) the spectral character of the 2D and 3D fields arising from these dynamics, and
4) the consequences of turbulence and mixing in such environments.

Here, we relate our results to previous modeling studies and measurements of such dynamics.

Interactions between the GW and FS fields in our DNSs are confined to modes that are periodic in our computational domain. Nevertheless, the initial superposition yields strong, off-resonant wave–wave interactions that diminish the initial GW and FS amplitudes by about 30%–40% within about $5T_b$–$10T_b$. These interactions are confined entirely to the plane of GW propagation (all modes have $l = l' = 0$) and are virtually identical in cases L0 and R prior to local instability and turbulence generation. This indicates that only the FS component in the GW plane contributes to these interactions at lowest order. Where the 2D FS is oblique or orthogonal to the GW, such interactions are weaker or nonexistent. The constraints of periodicity and a tilted domain are likely strong, in that true resonant interactions are highly unlikely, as each of three resonant modes would need to be periodic and the spectrum of allowed modes is quantized rather than quasi continuous, as in the atmosphere and oceans. Our tilted computational domain nevertheless allows a broad spectrum of GWs including modes having horizontal or vertical wavelengths far larger than the computational domain and thus frequencies in the range $0 \le \omega \le N$.

Despite the constraints of our computational domain, the observed interactions display a qualitative resemblance to resonant and off-resonant interactions described in the extensive literature cited above. Various studies showed a number of modes to arise rapidly and fill the available spectrum or to enable a flux of GW energy throughout an existing spectrum (e.g., see McComas and Bretherton 1977; Müller et al. 1986; Klostermeyer 1991; Vanneste 1995; Staquet and Sommeria 2002). Other studies revealed strong resonant or off-resonant interactions in confined periodic domains subjected to periodic forcing or sustained GW propagation (e.g., Thorpe 1994; Benielli and Sommeria 1998; Fritts et al. 2006). The primary difference between our DNS results and many previous studies is our initial superposition of two finite-amplitude GW and FS fields that enable rapid interactions among global, discrete rather than local, continuous GW fields. Without further evaluation of the influences of these discrete interactions, however, we cannot judge the relevance of our results fully. This would require exploration of these same dynamics in larger computational domains that would allow for more finely discretized spectra that are beyond the scope of the present study. The GW spectra that arise in our DNSs nevertheless allow ample exploration of the influences of GW and FS superpositions for instability dynamics and turbulence occurrence and effects, which are the primary foci of this and the companion study (Part II).

Instabilities arising within the GW–FS superpositions discussed here are seen to comprise three primary types: 1) counterrotating, streamwise-aligned vortices at initial vorticity sheets having a local $N^2 < 0$ by virtue of FS advection in regions where the GW θ' gradient is in the direction of increasing FS velocity with height; 2) KHI at larger and smaller scales on strong vorticity sheets where $N^2 > 0$, $\mathrm{Ri} < 1/4$, and Re is sufficiently large; and 3) GW breaking and plunging motions (at larger GW amplitudes) or fluid intrusions (at smaller GW amplitudes) that account for much of the turbulence generation at later stages of our various DNSs.

As noted in section 3b, the first of these instability types is closely analogous to the secondary instability of KH billows identified in stability analyses of these flows (Klaassen and Peltier 1985), in the laboratory (Thorpe 1985), and in multiple numerical studies of KHI for various flow parameters (Caulfield and Peltier 1994; Palmer et al. 1994, 1996; Fritts et al. 1996, 2003, 2012; Werne and Fritts 1999, 2001; Smyth et al. 2005; Werne et al. 2005). It also bears a close resemblance to Langmuir circulations in the ocean mixed layer, to roll vortices observed in the convective boundary layer, and to the primary instability accounting for GW breaking at sufficiently large GW amplitudes (e.g., Fritts et al. 1994, 1996, 1998, 2009b; Winters and D'Asaro 1994). As a secondary instability within KHI, it exhibits a strong increase of spanwise wavenumber and growth rate with decreasing Ri and increasing Re. Given the apparent ubiquity of this instability type in various transitional and boundary layer flows, it is not surprising that it also appears to play a primary instability role at free shear layers yielding similar environments.

The second instability type, KHI, is equally as pervasive throughout the atmosphere and oceans as it is in our DNSs discussed here. KHI is frequently observed at horizontal scales ranging from a few meters or less in the SBL and ocean thermocline to approximately 10 km or greater in the MLT. Small Ri ($\ll$1/4) and large Re (Re = $UL/\nu \sim 1000$ or greater, where U and L are the half-velocity difference and half the depth of the initial shear layer) yield deep KH billows, rapid instability and turbulence evolution, and strong local mixing. Larger Ri ($<$1/4) and/or smaller Re yield shallow KH billows, different secondary instability character, or no turbulence transition if Re $\sim$ 300 or less (Fritts and Rastogi 1985; Thorpe 1987). Observations in the troposphere, stratosphere, and MLT, where KH billow scales are sufficiently large to be observed by radar, lidar, and in airglow or noctilucent cloud imaging, often reveal relatively deep KH billows indicative of a small Ri and large Re, strong turbulence generation, and descending large-scale motions, as seen in our DNSs from $t \sim 11.5T_b$ to $12.5T_b$ in Figs. 6, 9, and 12. Examples include radar backscatter indicating deep billows with apparently well-mixed cores (Fritts and Rastogi 1985 and references therein; Lehmacher et al. 2007; Woodman et al. 2007; Luce et al. 2008; Fukao et al. 2011), lidar measurements of deep KH billows and their descent with time (Pfrommer et al. 2009) and airglow observations of KH billows and secondary instabilities (Hecht et al. 2005).

The third instability type noted in our GW–FS DNS includes GW breaking and fluid intrusions that arise where superposed GW and FS motions achieve maxima in the direction of GW propagation. This was seen to be the dominant large-scale source of turbulence at later stages in our various DNS evolutions. Our DNS prevalence of this instability is consistent with the inferred (and observed) role of GW breaking extending throughout the atmosphere, especially in the MLT. Indeed, we should expect GW breaking to play an even more dominant role in the atmosphere, where density decreases with altitude and large-scale wind shears (neither of which occurs in our DNS cases) can induce large local GW amplitudes. Nevertheless, our DNS evidence for intrusions as a significant cause of turbulence at smaller GW amplitudes provides a motivation to look more closely at observational data for evidence of these instabilities as well. Examples of measurements establishing the importance of GW breaking throughout the atmosphere include specific evidence of large-scale overturning in measurements of mountain wave structures during downslope wind storms (e.g., Lilly and Kennedy 1973; Lilly 1978); similar larger-scale overturning features in θ profiles inferred from lidar, falling-sphere, and balloon measurements at higher altitudes; and numerous measurements of GW momentum flux profiles exhibiting strong divergence and implied GW dissipation and mean-flow forcing (Fritts and Alexander 2003 and references therein).

The wave–wave interactions and instabilities occurring in our DNSs yield horizontal and vertical wavenumber spectra of velocities and θ' that exhibit large differences between 2D GW and 3D turbulence fields. Both 2D k' and m' spectra reveal clear approximately -3 slopes at larger scales, while the corresponding 3D spectra exhibit slopes of approximately $-5/3$ at scales smaller than the crossover wavenumbers in each case. These transitions in slope closely resemble those seen in atmospheric and oceanic spectra spanning the transition from the "saturated GW" range to the turbulence inertial range seen in multiple observations and anticipated by various GW saturation theories (e.g., Gargett et al. 1981; Dewan and Good 1986; Smith et al. 1987; Tsuda et al. 1989; Hines 1991; Fritts and Alexander 2003). Similar slope transitions are also anticipated in, and observed in DNSs of, stratified turbulence (e.g., Riley and Lindborg 2007; Almalkie and de Bruyn Kops 2012). However, our spectra at scales larger than the transition scale [$L_O \sim (\varepsilon/N^3)^{1/2}$, for vertical spectra] do not appear to include significant quasi-horizontal 3D motions having $l \neq 0$ and horizontal greater than vertical TKE.

5. Summary and conclusions

We performed a set of four DNSs of GW–FS interactions employing a common GW, but having different initial FS flows, to study idealized multiscale instability and turbulence dynamics. These DNSs were motivated by the ubiquitous occurrence of multiscale flows from the stable boundary layer into the lower thermosphere. The initial GW had a horizontal velocity amplitude of $a = u_0'/c = 0.5$, a frequency of $\omega = N/10$, and a wavelength λ_{GW} equal to the depth of the computational domain aligned along the GW group velocity. Three DNS employed a FS horizontal wind $V(z) = (2N/m_{FS})\sin(m_{FS}z)$, with $m_{FS} = 2\pi/\lambda_{FS}$ and $\lambda_{FS} \sim \lambda_{GW}/5$ in planes oriented at 0°, 45°, and 90° to the plane of GW propagation. A fourth DNS imposed a rotary initial FS wind field having equal magnitudes in each plane. All DNS were performed for Re $= \lambda_z^2/T_b\nu = 50\,000$ to allow vigorous instability and turbulence dynamics. In each case, the GW had a minimum Ri $\sim$ 4 and the FS had a minimum Ri = 1/4. Thus each field alone was stable over short times, but the superposition had a minimum initial Ri $\sim$ 1/8 in the least stable phase of the GW.

The four DNSs reveal that multiscale instabilities and turbulence are highly dependent on the relative orientation of the GW and the FS. The two cases with linear FS at 0° to the plane of GW propagation and rotary FS exhibit strong instability and turbulence dynamics, but the linear FSs oriented at 45° and 90° yield weak and no instability, respectively. Hence, our discussion here focuses only on the 0° linear and rotary FS cases, denoted cases L0 and R.

Despite the simplicity of the initial conditions, mutual deformations of the GW and FS fields lead quickly to 2D wave–wave interactions in the plane of GW propagation that are essentially identical in cases L0 and R. These interactions reduce the initial GW amplitude by about 30%–40% within about $5T_b$–$10T_b$ ($\sim 0.5T_{\rm GW}$–$1T_{\rm GW}$), after which it remains nearly unchanged for the duration of each DNS. FS velocity variances are also effectively transferred to high-m' GW motions during this time owing to the strong streamwise modulations of these flow features.

Unlike the 2D wave–wave interactions, initial instability onset differs significantly in cases L0 and R owing to suppression of initial instabilities occurring in case L0 by spanwise FS shears in case R. The different FS shears also lead to quite different initial instability dynamics in the two cases. Case L0 exhibits a symmetric initial instability comprising streamwise-aligned counterrotating vortices that arises quickly following initial overturning at the sites of strong FS advection of the GW θ' field. Initial instabilities in case R, in contrast, are delayed by about $1T_b$ and arise initially on highly distorted vorticity sheets accompanying initial large-scale overturning.

Following widespread turbulence generation in cases L0 and R, however, the two evolutions proceed closely in parallel. Instabilities at later stages are essentially of three types. KHI forms at larger and smaller scales on strong vorticity sheets throughout the two DNSs, initial GW breaking is replaced by fluid intrusions leading to turbulence generation extending to late times, and initial instabilities comprising streamwise-aligned counterrotating vortices arise where FS advection of the GW field yields local overturning. The latter of these instabilities is strongly suppressed in case R initially by spanwise FS shears. Instabilities and turbulence in the two cases typically occur at approximately the same sites, given primary control of the instability dynamics by the 2D GW field common to both cases. They also exhibit similar forms, but with differences in the timing, forms, and detailed structures due to minor variations in the 2D fields and the influences of the spanwise FS.

Control of instability and turbulence occurrence and statistics by the larger-scale superposition of GWs yields intermittent and localized turbulence sources that resemble observations more closely than more idealized DNSs addressing either KHI or monochromatic GW breaking alone. Layering of instabilities and turbulence in cases L0 and R also lead to persistent "sheet and layer" structures in θ, which bear a close resemblance to measurements throughout the atmosphere and in the oceans. Thus, idealized DNSs of GW–FS interactions reproduce several key aspects of such flows in the atmosphere and oceans. Additional comparisons and agreements are identified in the dissipation fields accompanying these dynamics in the companion paper (Part II).

The close correspondence of small-scale dynamics and instabilities seen in our GW–FS DNS cases and those seen throughout the atmosphere (and in the oceans) give us confidence that such modeling studies will prove valuable in interpreting existing and new observations and planning for future measurement programs. These similarities likely arise because of the multiscale wave–wave interactions, with details that depend on the specific flows, but consequences for local instabilities that are common to all such flows. In particular, we anticipate that increasingly realistic DNSs will yield an improved ability to quantify the character and effects of turbulence events and the relations among various turbulence quantities that remain poorly defined at present.

Acknowledgments. Support for this research was provided by the Army Research Office under Contract W911NF-12-C-0097, NASA under Contract NNH09CF40C, and the National Science Foundation under Grants AGS-1242943, AGS-1242949, and AGS-1250454. We gratefully acknowledge access to large computational resources provided by the DoD High Performance Computing Modernization Office for our various studies.

REFERENCES

Achatz, U., 2005: On the role of optimal perturbations in the instability of monochromatic gravity waves. *Phys. Fluids,* **17,** 094107, doi:10.1063/1.2046709.

——, 2007: The primary nonlinear dynamics of modal and nonmodal perturbations of monochromatic inertia–gravity waves. *J. Atmos. Sci.,* **64,** 74–95.

——, and G. Schmitz, 2006a: Shear and static instability of inertia–gravity wave packets: Short-term modal and nonmodal growth. *J. Atmos. Sci.,* **63,** 397–413.

——, and ——, 2006b: Optimal growth in inertia–gravity wave packets: Energetics, long-term development, and three-dimensional structure. *J. Atmos. Sci.,* **63,** 414–434.

Almalkie, S., and S. M. de Bruyn Kops, 2012: Kinetic energy dynamics in forced, homogeneous, and axisymmetric stably stratified turbulence. *J. Turbul.,* **13,** N29, doi:10.1080/14685248.2012.702909.

Andreassen, Ø., C.-E. Wasberg, D. C. Fritts, and J. R. Isler, 1994: Gravity wave breaking in two and three dimensions: 1. Model description and comparison of two-dimensional evolutions. *J. Geophys. Res.,* **99** (D4), 8095–8108.

——, P. O. Hvidsten, D. C. Fritts, and S. Arendt, 1998: Vorticity dynamics in a breaking internal gravity wave. Part 1. Initial instability evolution. *J. Fluid Mech.,* **367,** 27–46.

Arendt, S., D. C. Fritts, and Ø. Andreassen, 1997: The initial value problem for Kelvin vortex waves. *J. Fluid Mech.,* **344,** 181–212.

——, ——, and ——, 1998: Kelvin twist waves in the transition to turbulence. *Eur. J. Mech.,* **17B,** 595–604.

Balsley, B. B., M. L. Jensen, and R. Frehlich, 1998: The use of state-of-the-art kites for profiling the lower atmosphere. *Bound.-Layer Meteor.,* **87,** 1–25.

——, R. G. Frehlich, M. L. Jensen, Y. Meillier, and A. Muschinski, 2003: Extreme gradients in the nocturnal boundary layer: Structure, evolution, and potential causes. *J. Atmos. Sci.,* **60,** 2496–2508.

——, ——, ——, ——, and ——, 2006: High-resolution in situ profiling through the stable boundary layer: Examination of the SBLtop in terms of minimum shear, maximum stratification, and turbulence decrease. *J. Atmos. Sci.,* **63,** 1291–1307.

——, D. A. Lawrence, R. F. Woodman, and D. C. Fritts, 2012: Fine-scale characteristics of temperature, wind, and turbulence in the lower atmosphere (0–1,300 m) over the south Peruvian coast. *Bound.-Layer Meteor.,* **147,** 165–178, doi:10.1007/s10546-012-9774-x.

Barat, J., 1982: Some characteristics of clear-air turbulence in the middle atmosphere. *J. Atmos. Sci.,* **39,** 2553–2564.

——, C. Cot, and C. Sidi, 1984: On the measurement of the turbulence dissipation rate from rising balloons. *J. Atmos. Oceanic Technol.,* **1,** 270–275.

Benielli, D., and J. Sommeria, 1998: Excitation and breaking of internal gravity waves by parametric instability. *J. Fluid Mech.,* **374,** 117–144.

Bouruet-Aubertot, P., J. Sommeria, and C. Staquet, 1995: Breaking of standing internal gravity waves through two-dimensional instabilities. *J. Fluid Mech.,* **285,** 265–301.

Caulfield, C. P., and W. R. Peltier, 1994: Three dimensionalization of the stratified mixing layer. *Phys. Fluids,* **6,** 3803–3805.

Chau, J. L., R. J. Doviak, A. Muschinski, and C. L. Holloway, 2000: Lower atmospheric measurements of turbulence and characteristics of Bragg scatterers, using the Jicamarca VHF radar. *Radio Sci.,* **35,** 179–193.

Coulman, C. E., J. Vernin, and A. Fuchs, 1995: Optical seeing mechanism of formation of thin turbulent laminae in the atmosphere. *Appl. Opt.,* **34,** 5461–5474.

Craik, A. D. D., 1985: *Wave Interactions and Fluid Flow.* Cambridge University Press, 336 pp.

Dalaudier, F., C. Sidi, M. Crochet, and J. Vernin, 1994: Direct evidence of "sheets" in the atmospheric temperature field. *J. Atmos. Sci.,* **51,** 237–248.

Dewan, E. M., and R. E. Good, 1986: Saturation and the "universal" spectrum for vertical profiles of horizontal scalar winds in the atmosphere. *J. Geophys. Res.,* **91,** 2742–2748.

Dillon, T. M., 1982: Vertical overturns: A comparison of Thorpe and Ozmidov length scales. *J. Geophys. Res.,* **87** (C12), 9601–9613.

Dosser, H. V., and B. R. Sutherland, 2011: Weakly nonlinear non-Boussinesq internal gravity wave packets. *Physica D,* **240,** 346–356.

Drazin, P. G., 1977: On the instability of an internal gravity wave. *Proc. Roy. Soc. London,* **A356,** 411–432.

Eaton, F., S. A. Mclaughlin, and J. R. Hines, 1995: A new frequency-modulated continuous wave radar for studying planetary boundary layer morphology. *Radio Sci.,* **30,** 75–88.

Franke, P. M., S. Mahmoud, K. Raizada, K. Wan, D. C. Fritts, T. Lund, and J. Werne, 2011: Computation of clear-air radar backscatter from numerical simulations of turbulence: 1. Numerical methods and evaluation of biases. *J. Geophys. Res.,* **116,** D21101, doi:10.1029/2011JD015895.

Fritts, D. C., and P. K. Rastogi, 1985: Convective and dynamical instabilities due to gravity wave motions in the lower and middle atmosphere: Theory and observations. *Radio Sci.,* **20,** 1247–1277.

——, and M. J. Alexander, 2003: Gravity dynamics and effects in the middle atmosphere. *Rev. Geophys.,* **41,** 1003, doi:10.1029/2001RG000106.

——, and T. Lund, 2011: Gravity wave influences in the thermosphere and ionosphere: Observations and recent modeling. *Aeronomy of the Earth's Atmosphere and Ionosphere,* M. Abdu and D. Pancheva, Eds., Springer, 109–130.

——, and L. Wang, 2013: Gravity wave–fine structure interactions. Part II: Energy dissipation evolutions, statistics, and implications. *J. Atmos. Sci.,* **70,** 3735–3755.

——, J. R. Isler, and Ø. Andreassen, 1994: Gravity wave breaking in two and three dimensions: 2. Three-dimensional evolution and instability structure. *J. Geophys. Res.,* **99** (D4), 8109–8123.

——, J. F. Garten, and Ø. Andreassen, 1996: Wave breaking and transition to turbulence in stratified shear flows. *J. Atmos. Sci.,* **53,** 1057–1085.

——, S. Arendt, and Ø. Andreassen, 1998: Vorticity dynamics in a breaking internal gravity wave. Part 2. Vortex interactions and transition to turbulence. *J. Fluid Mech.,* **367,** 47–65.

——, C. Bizon, J. A. Werne, and C. K. Meyer, 2003: Layering accompanying turbulence generation due to shear instability and gravity-wave breaking. *J. Geophys. Res.,* **108** (D8), 8452, doi:10.1029/2002JD002406.

——, and Coauthors, 2004: Observations of extreme temperature and wind gradients near the summer mesopause during the MaCWAVE/MIDAS rocket campaign. *Geophys. Res. Lett.,* **31,** L24S06, doi:10.1029/2003GL019389.

——, S. L. Vadas, K. Wan, and J. A. Werne, 2006: Mean and variable forcing of the middle atmosphere by gravity waves. *J. Atmos. Sol. Terr. Phys.,* **68,** 247–265.

——, L. Wang, J. Werne, T. Lund, and K. Wan, 2009a: Gravity wave instability dynamics at high Reynolds numbers. Part I: Wave field evolution at large amplitudes and high frequencies. *J. Atmos. Sci.,* **66,** 1126–1148.

——, ——, ——, ——, and ——, 2009b: Gravity wave instability dynamics at high Reynolds numbers. Part II: Turbulence evolution, structure, and anisotropy. *J. Atmos. Sci.,* **66,** 1149–1171.

——, ——, and ——, 2009c: Gravity wave–fine structure interactions: A reservoir of small-scale and large-scale turbulence energy. *Geophys. Res. Lett.,* **36,** L19805, doi:10.1029/2009GL039501.

——, P. Franke, K. Wan, T. Lund, and J. Werne, 2011: Computation of clear-air radar backscatter from numerical simulations of turbulence: 2. Backscatter moments throughout the lifecycle of a Kelvin-Helmholtz instability. *J. Geophys. Res.,* **116,** D11105, doi:10.1029/2010JD014618.

——, K. Wan, P. Franke, and T. Lund, 2012: Computation of clear-air radar backscatter from numerical simulations of turbulence: 3. Off-zenith measurements and biases throughout the lifecycle of a Kelvin-Helmholtz instability. *J. Geophys. Res.,* **117,** D17101, doi:10.1029/2011JD017179.

Fukao, S., H. Luce, T. Mega, and M. K. Yamamoto, 2011: Extensive studies of large-amplitude Kelvin–Helmholtz billows in the lower atmosphere with VHF middle and upper atmosphere radar. *Quart. J. Roy. Meteor. Soc.,* **137,** 1019–1041, doi:10.1002/qj.807.

Gargett, A. E., P. J. Hendricks, T. B. Sanford, T. R. Osborn, and A. J. Williams, 1981: A composite spectrum of vertical shear in the upper ocean. *J. Phys. Oceanogr.,* **11,** 1258–1271.

Gavrilov, N. M., H. Luce, M. Crochet, F. Dalaudier, and S. Fukao, 2005: Turbulence parameter estimations from high-resolution balloon temperature measurements of the MUTSI-2000 campaign. *Ann. Geophys.,* **23,** 2401–2413.

Goldberg, and Coauthors, 2006: The MaCWAVE program to study gravity wave influences on the polar mesosphere. *Ann. Geophys.,* **24,** 1159–1173.

Gossard, E. E., D. R. Jensen, and J. H. Richter, 1971: An analytical study of tropospheric structure as seen by high-resolution radar. *J. Atmos. Sci.,* **28,** 794–807.

——, W. D. Neff, R. J. Zamora, and J. E. Gaynor, 1984: The fine structure of elevated refractive layers: Implications for over-the-horizon propagation and radar sounding systems. *Radio Sci.,* **19,** 1523–1533.

——, J. E. Gaynor, R. J. Zamora, and W. D. Neff, 1985: Fine structure of elevated stable layers observed by sounder and in-situ tower sensors. *J. Atmos. Sci.,* **42,** 2156–2169.

Gregg, M. C., and M. G. Briscoe, 1979: Internal waves, finestructure, microstructure, and mixing in the ocean. *Rev. Geophys.,* **17,** 1524–1548, doi:10.1029/RG017i007p01524.

Hecht, J. H., A. Z. Liu, R. L. Walterscheid, and R. J. Rudy, 2005: Maui Mesosphere and Lower Thermosphere (Maui MALT) observations of the evolution of Kelvin-Helmholtz billows formed near 86 km altitude. *J. Geophys. Res.,* **110,** D09S10, doi:10.1029/2003JD003908.

Hines, C. O., 1991: The saturation of gravity waves in the middle atmosphere. Part I: Critique of linear-instability theory. *J. Atmos. Sci.,* **48,** 1348–1359.

Julien, K., S. Legg, J. McWillimas, and J. Werne, 1996: Rapidly rotating turbulent Rayleigh-Bénard convection. *J. Fluid Mech.,* **322,** 243–273.

Kelley, M. C., C. Y. Chen, R. R. Beland, R. Woodman, J. L. Chau, and J. Werne, 2005: Persistence of a Kelvin-Helmholtz instability complex in the upper troposphere. *J. Geophys. Res.,* **110,** D14106, doi:10.1029/2004JD005345.

Klaassen, G. P., and W. R. Peltier, 1985: The onset of turbulence in finite-amplitude Kelvin-Helmholtz billows. *J. Fluid Mech.,* **155,** 1–35.

Klostermeyer, J., 1982: On parametric instabilities of finite-amplitude internal gravity waves. *J. Fluid Mech.,* **119,** 367–377.

——, 1991: Two- and three-dimensional parametric instabilities in finite amplitude internal gravity waves. *Geophys. Astrophys. Fluid Dyn.,* **64,** 1–25.

Koudella, C. R., and C. Staquet, 2006: Instability mechanisms of a two-dimensional progressive internal gravity wave. *J. Fluid Mech.,* **548,** 165–196.

LeBlond, P. H., and L. A. Mysak, Eds., 1978: *Waves in the Ocean.* Elsevier Oceanography Series, Vol. 20, Elsevier, 602 pp.

Lehmacher, G. A., L. Guo, E. Kudeki, P. M. Reyes, A. Akgiray, and J. L. Chau, 2007: High-resolution observations of mesospheric layers with the Jicamarca VHF radar. *Adv. Space Res.,* **40,** 734–743.

Lelong, M.-P., and T. J. Dunkerton, 1998a: Inertia–gravity wave breaking in three dimensions. Part I: Convectively stable waves. *J. Atmos. Sci.,* **55,** 2473–2488.

——, and ——, 1998b: Inertia–gravity wave breaking in three dimensions. Part II: Convectively unstable waves. *J. Atmos. Sci.,* **55,** 2489–2501.

Li, F., A. Z. Liu, G. R. Swenson, J. H. Hecht, and W. A. Robinson, 2005: Observations of gravity wave breakdown into ripples associated with dynamical instabilities. *J. Geophys. Res.,* **110,** D09S11, doi:10.1029/2004JD004849.

Lilly, D. K., 1978: A severe downslope windstorm and aircraft turbulence event induced by a mountain wave. *J. Atmos. Sci.,* **35,** 59–77.

——, and P. J. Kennedy, 1973: Observations of a stationary mountain wave and its associated momentum flux and energy dissipation. *J. Atmos. Sci.,* **30,** 1135–1152.

Lombard, P. N., and J. J. Riley, 1996: Instability and breakdown of internal gravity waves. I. Linear stability analysis. *Phys. Fluids,* **8,** 3271–3287.

Lübken, F.-J., M. Rapp, and P. Hoffmann, 2002: Neutral air turbulence and temperatures in the vicinity of polar mesosphere summer echoes. *J. Geophys. Res.,* **107** (D15), doi:10.1029/2001JD000915.

Luce, H., M. Crochet, F. Dalaudier, and C. Sidi, 1995: Interpretation of VHF ST radar vertical echoes from in situ temperature sheet observations. *Radio Sci.,* **30,** 1002–1025.

——, ——, ——, and ——, 2001: Temperature sheets and aspect sensitive radar echoes. *Ann. Geophys.,* **19,** 899–920.

——, S. Fukao, F. Dalaudier, and M. Crochet, 2002: Strong mixing events observed near the tropopause with the MU radar and high-resolution balloon techniques. *J. Atmos. Sci.,* **59,** 2885–2896.

——, G. Hassenpflug, M. Yamamoto, M. Crochet, and S. Fukao, 2007: Range-imaging observations of cumulus convection and Kelvin-Helmholtz instabilities with the MU radar. *Radio Sci.,* **42,** RS1005, doi:10.1029/2005RS003439.

——, ——, ——, S. Fukao, and K. Sato, 2008: High-resolution observations with MU radar of a KH instability triggered by an inertia–gravity wave in the upper part of a jet stream. *J. Atmos. Sci.,* **65,** 1711–1718.

Lund, T. S., and D. C. Fritts, 2012: Numerical simulation of gravity wave breaking in the lower thermosphere. *J. Geophys. Res.,* **117,** D21105, doi:10.1029/2012JD017536.

Mahrt, L., 1999: Stratified atmospheric boundary layers. *Bound.-Layer Meteor.,* **90,** 375–396, doi:10.1023/A:1001765727956.

McComas, C. H., and F. P. Bretherton, 1977: Resonant interactions of oceanic internal waves. *J. Geophys. Res.,* **82,** 1397–1411.

McEwan, A. D., 1971: Degeneration of resonantly excited standing internal gravity waves. *J. Fluid Mech.,* **50,** 431–448.

——, and A. Plumb, 1977: Off-resonant amplification of finite internal wave packets. *Dyn. Atmos. Oceans,* **2,** 83–105.

Mied, R. P., 1976: The occurrence of parametric instabilities in finite-amplitude internal gravity waves. *J. Fluid Mech.,* **78,** 763–784.

Müller, P., G. Holloway, F. Henyey, and N. Pomphrey, 1986: Nonlinear interactions among internal gravity waves. *Rev. Geophys.,* **24,** 492–536.

Muschinski, A., and C. Wode, 1998: First in situ evidence for coexisting submeter temperature and humidity sheets in the lower free troposphere. *J. Atmos. Sci.,* **55,** 2893–2906.

——, P. B. Chilson, S. Kern, J. Nielinger, G. Schmidt, and T. Prenosil, 1999: First frequency-domain interferometry observations of large-scale vertical motion in the atmosphere. *J. Atmos. Sci.,* **56,** 1248–1258.

Nastrom, G. D., and F. D. Eaton, 2001: Persistent layers of enhanced C_n^2 in the lower stratosphere from radar. *Radio Sci.,* **36,** 137–149.

Orlanski, I., 1972: On the breaking of standing internal gravity waves. *J. Fluid Mech.,* **54,** 577–598.

——, and C. P. Cerasoli, 1981: Energy transfer among internal gravity modes: Weak and strong. *J. Geophys. Res.,* **86** (C5), 4103–4124.

Palmer, T. L., D. C. Fritts, Ø. Andreassen, and I. Lie, 1994: Three-dimensional evolution of Kelvin-Helmholtz billows in stratified compressible flow. *Geophys. Res. Lett.,* **21,** 2287–2290.

——, ——, and ——, 1996: Evolution and breakdown of Kelvin–Helmholtz billows in stratified compressible flows. Part II:

Instability structure, evolution, and energetics. *J. Atmos. Sci.,* **53,** 3192–3212.

Pfrommer, T., P. Hickson, and C.-Y. She, 2009: A large-aperture sodium fluorescence lidar with very high resolution for mesopause dynamics and adaptive optics studies. *Geophys. Res. Lett.,* **36,** L15831, doi:10.1029/2009GL038802.

Phillips, O. M., 1977: *The Dynamics of the Upper Ocean.* 2nd ed. Cambridge University Press, 344 pp.

——, 1981: Wave interactions—The evolution of an idea. *J. Fluid Mech.,* **106,** 215–227.

Rapp, M., F.-J. Lübken, A. Müllemann, G. E. Thomas, and E. J. Jensen, 2002: Small-scale temperature variations in the vicinity of NLC: Experimental and model results. *J. Geophys. Res.,* **107,** 4392, doi:10.1029/2001JD001241.

——, B. Strelnikov, A. Müllemann, F.-J. Lübken, and D. C. Fritts, 2004: Turbulence measurements implications for gravity wave dissipation during the MaCWAVE/MIDAS summer rocket program. *Geophys. Res. Lett.,* **31,** L24S07, doi:10.1029/2003GL019325.

Riley, J. J., and E. Lindborg, 2007: Stratified turbulence: A possible interpretation of some geophysical turbulence measurements. *J. Atmos. Sci.,* **65,** 2416–2424.

Seim, H. E., and M. C. Gregg, 1994: Detailed observations of a naturally occurring shear instability. *J. Geophys. Res.,* **99** (C5), 10 049–10 073.

Smith, S. A., D. C. Fritts, and T. E. VanZandt, 1987: Evidence for a saturated spectrum of atmospheric gravity waves. *J. Atmos. Sci.,* **44,** 1404–1410.

Smyth, W. D., J. D. Nash, and J. N. Moun, 2005: Differential diffusion in breaking Kelvin–Helmholtz billows. *J. Phys. Oceanogr.,* **35,** 1004–1022.

Sonmor, L. J., and G. P. Klaassen, 1997: Toward a unified theory of gravity wave stability. *J. Atmos. Sci.,* **54,** 2655–2680.

Sorbjan, Z., and B. B. Balsley, 2008: Microstructure of turbulence in the stably stratified boundary layer. *Bound.-Layer Meteor.,* **129,** 191–210, doi:10.1007/s10546-008-9310-1.

Spalart, P. R., R. D. Moser, and M. M. Rogers, 1991: Spectral methods for the Navier-Stokes equations with one infinite and two periodic directions. *J. Comput. Phys.,* **96,** 297–324.

Staquet, C., and J. Sommeria, 2002: Internal gravity waves: From instability to turbulence. *Annu. Rev. Fluid Mech.,* **34,** 559–593.

Sutherland, B. R., 2001: Finite-amplitude internal wavepacket dispersion and breaking. *J. Fluid Mech.,* **429,** 343–380.

——, 2006a: Internal wave instability: Wave-wave versus wave-induced mean flow interactions. *Phys. Fluids,* **18,** 074107, doi:10.1063/1.2219102.

——, 2006b: Weakly nonlinear internal gravity wavepackets. *J. Fluid Mech.,* **569,** 249–258.

Thorpe, S. A., 1968: On standing internal gravity waves of finite amplitude. *J. Fluid Mech.,* **32,** 489–528.

——, 1977: Turbulence and mixing in a Scottish loch. *Philos. Trans. Roy. Soc. London,* **A286,** 125–181.

——, 1985: Laboratory observations of secondary structures in Kelvin-Helmholtz billows and consequences for ocean mixing. *Geophys. Astrophys. Fluid Dyn.,* **34** (1–4), 175–199.

——, 1987: Transitional phenomena and the development of turbulence in stratified fluids: A review. *J. Geophys. Res.,* **92** (C5), 5231–5248.

——, 1994: Observations of parametric instability and breaking waves in an oscillating tilted tube. *J. Fluid Mech.,* **261,** 33–45.

——, 1999: On the breaking of internal waves in the ocean. *J. Phys. Oceanogr.,* **29,** 2433–2441.

Tsuda, T., T. Inoue, D. C. Fritts, T. E. VanZandt, S. Kato, T. Sato, and S. Fukao, 1989: MST radar observations of a saturated gravity wave spectrum. *J. Atmos. Sci.,* **46,** 2440–2447.

——, S. Kato, T. Yokoi, T. Inoue, M. Yamamoto, T. E. VanZandt, S. Fukao, and T. Sato, 1990: Gravity waves in the mesosphere observed with the middle and upper atmosphere radar. *Radio Sci.,* **25,** 1005–1018.

Vanneste, J., 1995: The instability of internal gravity waves to localized disturbances. *Ann. Geophys.,* **13,** 196–210.

VanZandt, T. E., J. L. Green, K. S. Gage, and W. L. Clark, 1978: Vertical profiles of refractivity turbulence structure constant: comparison of observations by the Sunset Radar with a new theoretical model. *Radio Sci.,* **13,** 819–829.

Wang, L., D. C. Fritts, B. P. Williams, R. A. Goldberg, F. J. Schmidlin, and U. Blum, 2006: Gravity waves in the middle atmosphere during the MaCWAVE winter campaign: Evidence of mountain wave critical level encounters. *Ann. Geophys.,* **24,** 1209–1226.

Werne, J., and D. C. Fritts, 1999: Stratified shear turbulence: Evolution and statistics. *Geophys. Res. Lett.,* **26,** 439–442.

——, and ——, 2001: Anisotropy in a stratified shear layer. *Phys. Chem. Earth,* **26B,** 263–268.

——, T. Lund, B. A. Pettersson-Reif, P. Sullivan, and D. C. Fritts, 2005: CAP phase II simulations for the Air Force HEL-JTO project: Atmospheric turbulence simulations on NAVO's 3000-processor IBM P4+ and ARL's 2000-processor Intel Xeon EM64T cluster. *Proc., 15th Department of Defense High Performance Computing Modernization Program Users Group Conf.,* Nashville, TN, DoD, 100–111.

Winters, K. B., and E. A. D'Asaro, 1994: 3D wave breaking near a critical level. *J. Fluid Mech.,* **272,** 255–284.

Woodman, R. F., G. Michhue, J. Roettger, and O. Castillo, 2007: The MPI-SOUSY-VHF radar at Jicamarca: High altitude-resolution capabilities. *Extended Abstracts, 11th International Workshop on Technical and Scientific Aspects of MST Radar,* Gadanki, India, Department of Science and Technology, Government of India, 4 pp.

Woods, J. D., 1968: Wave-induced shear instability in the summer thermocline. *J. Fluid Mech.,* **32,** 791–800.

——, 1969: On Richardson's number as a criterion for laminar-turbulent-laminar transition in the ocean and atmosphere. *Radio Sci.,* **4,** 1289–1298.

——, and R. L. Wiley, 1972: Billow turbulence and ocean microstructure. *Deep-Sea Res.,* **19,** 87–121.

Yamada, Y., H. Fukunishi, T. Nakamura, and T. Tsuda, 2001: Breaking of small-scale gravity wave and transition to turbulence observed in OH airglow. *Geophys. Res. Lett.,* **28,** 2153–2156.

Yeh, K. C., and C. H. Liu, 1981: The instability of atmospheric gravity waves through wave-wave interactions. *J. Geophys. Res.,* **86** (C10), 9722–9728.